Incorporating Diagnosed Intercept Parameters and the Graupel Category within the ARPS Cloud Analysis System for the Initialization of Double-Moment Microphysics: Testing with a Squall Line over South China

YUJIE PAN

Collaborative Innovation Center on Forecast and Evaluation of Meteorological Disasters/Key Laboratory of Meteorological Disaster, Ministry of Education, Nanjing University of Information Science and Technology, Nanjing, China, and Center for Analysis and Prediction of Storms, University of Oklahoma, Norman, Oklahoma

MING XUE

Center for Analysis and Prediction of Storms, and School of Meteorology, University of Oklahoma, Norman, Oklahoma, and School of Atmospheric Sciences, Nanjing University, Nanjing, China

GUOQING GE

Center for Analysis and Prediction of Storms, University of Oklahoma, Norman, Oklahoma

(Manuscript received 14 January 2015, in final form 22 September 2015)

ABSTRACT

In this study, a new set of reflectivity equations are introduced into the Advanced Regional Prediction System (ARPS) cloud analysis system. This set of equations incorporates double-moment microphysics information in the analysis by adopting a set of diagnostic relationships between the intercept parameters and the corresponding mass mixing ratios. A reflectivity- and temperature-based graupel classification scheme is also implemented according to a hydrometeor identification (HID) diagram. A squall line that occurred on 23 April 2007 over southern China containing a pronounced trailing stratiform precipitation region is used as a test case to evaluate the impacts of the enhanced cloud analysis scheme.

The results show that using the enhanced cloud analysis scheme is able to better capture the characteristics of the squall line in the forecast. The predicted squall line exhibits a wider stratiform region and a more clearly defined transition zone between the leading convection and the trailing stratiform precipitation region agreeing better with observations in general, when using the enhanced cloud analysis together with the two-moment microphysics scheme. The quantitative precipitation forecast skill score is also improved.

1. Introduction

Cloud microphysical processes strongly influence the structure, dynamics, and evolution of convective systems (Chin 1994; van den Heever and Cotton 2004; Grim et al. 2009; Smith et al. 2009; Rowe et al. 2012; Van Weverberg et al. 2013). These processes are currently parameterized in numerical weather prediction (NWP) models using either bulk or bin microphysics (MP) parameterization schemes. Bulk schemes specify a particle size distribution (PSD) for each hydrometer species and predict certain moments of PSD. Bin schemes predict the evolution of PSDs by discretizing the PSDs into multiple size bins thereby allowing much more flexibility in representing the hydrometeor sizes and the spectrum of fall speeds, etc. Bin schemes are, however, computationally much more expensive and often impractical in an operational context. Currently, bulk schemes are widely used in operational NWP models.

For a bulk scheme, cloud and precipitation PSDs are often represented by a gamma size distribution (Ulbrich 1983; Milbrandt and Yau 2005a):

$$N_x(D) = N_{0x}D^{\alpha_x}e^{-\lambda_x D}, \tag{1}$$

where N_x is the number concentration; N_{0x}, α_x, and λ_x are the intercept, shape, and slope parameters of the PSD,

Corresponding author address: Yujie Pan, School of Atmospheric Science, Nanjing University of Information Science and Technology, 219 Ningliu Rd., Nanjing, Jiangsu 210044, China.
E-mail: panyujie@gmail.com

respectively; and D is the particle diameter. Subscript x refers to one of the cloud/hydrometeor species. When $\alpha = 0$, the above gamma distribution reduces to an exponential distribution (Marshall and Palmer 1948):

$$N_x(D) = N_{0x}e^{-\lambda_x D}. \tag{2}$$

The pth moment of the PSD in (1) is

$$M_{x(p)} = \frac{N_{Tx}}{\lambda_x^p} \frac{\Gamma(1 + \alpha_x + p)}{\Gamma(1 + \alpha_x)}. \tag{3}$$

The zeroth moment of PSD is the total number concentration, the third moment is proportional to the mass mixing ratio, and the sixth moment is related to the reflectivity factor. In typical single-moment (SM) MP schemes (e.g., Kessler 1969; Lin et al. 1983; Milbrandt and Yau 2005a), the mass mixing ratios (q_x), which are monotonically related to fixed N_{0x}, are predicted. In reality, the latter is not the case. Previous studies (Straka et al. 2005; Dawson et al. 2010) have pointed it out that if the particles of a species were growing by aggregation or breakup, N_{0x} changes but q_x does not; and for accretion or diffusion, q_x changes but N_{0x} does not. In reality, the q_x and N_{0x} do not relate to each other monotonically. The computationally cheaper SM schemes should be improved in some way to better represent the real PSDs. One such effort is to allow for additional free parameters in the PSDs by adopting double-moment (DM) or triple-moment (TM) schemes that predict two or three PSD moments, respectively. Sensitivity studies (Ferrier 1994; Ferrier et al. 1995; Milbrandt and Yau 2005b; Dawson et al. 2010) suggest that multimoment schemes produce more realistic storm structures than SM schemes. The DM or TM schemes are, however, computationally more expensive, since they double or triple the number of prognostic variables associated with the species.

Another approach to improve SM schemes is to find certain relationship between q_x and N_{0x} so that only one moment has to be predicted but N_{0x} can still vary. Zhang et al. (2008) derived a diagnostic relationship between the intercept parameter and the water content based on two-dimensional video disdrometer (2DVD) measurements taken in Oklahoma during the summer seasons of 2005, 2006, and 2007. However, the relationship is for rainwater only and was derived from 2DVD surface measurements. For convective storm modeling, relationships for all precipitation species suitable for all levels are needed. Wainwright et al. (2014, hereafter W14) formulated and tested diagnostic relationships between the intercept parameter and water/ice content for rain, snow, graupel, and hail ($N_{0x} - W_x$ relations, where W_x is water/ice content, and x can be rain, snow,

graupel, and hail) based on the Milbrandt–Yau (MY) single- and multimoment MP scheme (Milbrandt and Yau 2005a,b) within the Advanced Regional Prediction System (ARPS; Xue et al. 2000; Xue et al. 2001). They derived the relationships from the ARPS three-dimensional (3D) simulation output using the DM MY scheme and demonstrated that the SM scheme employing the diagnostic instead of fixed N_{0x} can produce results close to those of the corresponding DM scheme.

The above finding is inspiring. In addition to employing the diagnostic $N_{0x} - W_x$ relationships within the MP parameterization schemes themselves, these schemes can be used to help with the analysis of microphysical states when assimilating radar reflectivity data, in a way that is consistent with the MP scheme used. Currently, radar reflectivity data assimilation remains a challenging problem. Sun and Crook (1997, 1998) assimilated radar reflectivity via the four-dimensional variational (4DVAR) analysis scheme. Their system, however, assumes warm rain MP only while strong nonlinearity associated with ice MP tends to create difficulties with 4DVAR minimization. In a three-dimensional variational (3DVAR) framework, direct assimilation of reflectivity requires additional assumptions (Gao and Stensrud 2012). Without direct links to other state variables in the observation operators or reliable background error cross covariances, direct assimilation of reflectivity data within a 3DVAR framework also tends to limit the direct data influence to the precipitation hydrometeors only in the analysis.

With the help of ensemble-derived flow-dependent background error covariance and in particular cross-variable covariance involving MP and other state variables, the ensemble Kalman filter (EnKF; Evensen 1994) technique has been shown to be able to estimate state variables associated with SM ice MP schemes (Tong and Xue 2005) from radar data. Tong and Xue (2008a,b) and Jung et al. (2010) further demonstrated successful estimation of PSD-related MP parameters, while Xue et al. (2010) and Jung et al. (2012) demonstrated that the EnKF is capable of estimating both mixing ratios and number concentrations associated with a two-moment MP scheme. The EnKF method is, however, computationally rather expensive, and for the convective scales has mostly been limited to non-real-time research applications at this time.

A computationally efficient alternative for assimilating the reflectivity data is the semiempirical cloud analysis method. A complex cloud analysis procedure is available within the ARPS system and has proven effective in many research studies (Xue et al. 2003; Hu et al. 2006a; Hu et al.

2006b; Schenkman et al. 2011) as well as in continental U.S. scale real-time forecasts (Xue et al. 2013). In the ARPS cloud analysis system, the hydrometeor mixing ratios are estimated from observed reflectivity based on two sets of reflectivity equations as alternative options. In the first set, the rainwater mixing ratio is retrieved using the Kessler reflectivity equation (Kessler 1969), and snow and hail are retrieved using the Rogers and Yau reflectivity formula (Rogers and Yau 1989). This set of equations or options will be referred to as KRY hereafter. The second set of equations retrieves precipitation mixing ratios according to the reflectivity formula defined in Smith et al. (1975). This set of equations will be referred as SMO and other details on the equations can be found in Tong and Xue (2005). Hu et al. (2006a) presented comparisons between these two options for the analysis of a supercell storm case. For the purpose of this study, we choose the SMO option as the reference for comparison with our enhanced scheme.

With both sets of equations, the intercept parameter for each hydrometeor PSD is assumed to be constant, as is typical of SM MP schemes. With this assumption, number concentrations associated with DM schemes might not be optimally initialized even when certain classification or partition schemes for the hydrometeors are devised. To initialize a DM MP forecast, both mass mixing ratios and total number concentrations are required. One possible solution to this problem is to utilize the diagnostic relations between the mixing ratios/water contents and the corresponding intercept parameters (Zhang et al. 2008). This allows for the diagnoses of the total number concentrations given the reflectivity contribution of a given species. As mentioned earlier, an SM scheme using such diagnostic relations has been shown to produce results close to (although not as good as) those of a DM scheme within a prediction model (W14). The application of such an approach within a data assimilation procedure is investigated in this study. The SM-based cloud analysis scheme within the ARPS modeling system is enhanced to do so.

Furthermore, both KRY and SMO formula used in the current ARPS cloud analysis system assume a hail category without graupel; the MY schemes that we will use in our study include both hail and graupel categories, and including both allows more realistic simulations of convective systems. This study will add the ability of analyzing the additional graupel category in the ARPS cloud analysis system. A simplified hydrometeor identification (HID) method will be used to help distinguish graupel.

To evaluate the impacts of our enhanced cloud analysis scheme on the analysis and forecasting of convective systems, a squall line from south China having a pronounced trailing stratiform precipitation region is chosen as the test case. Squall lines with trailing stratiform precipitation are common in both tropical and midlatitude regions, and have been studied by many authors (Zipser 1977; Moncrieff 1978; Houze et al. 1989; Biggerstaff and Houze1991; Rotunno et al. 1998; Parker and Johnson 2000; Weisman and Rotunno 2004). It has been found that classic mature squall lines usually have two distinct regions of precipitation separated by a transition zone of weaker precipitation: a convective region with heavy precipitation and a trailing stratiform region with moderate precipitation. The presence of the trailing stratiform and transition zones has been attributed to both fall speed sorting for particles originating from the top of convective cells (Rutledge and Houze 1987; Fovell and Ogura 1988; Biggerstaff and Houze 1993) and enhanced subsidence in the transition zone, which increases sublimation and evaporation (Smull and Houze 1985). Many studies have attempted to simulate the enhanced trailing stratiform region (Fovell and Ogura 1988; Gallus and Johnson 1995), but the region, even when obtained, tends to be too narrow and weak. The lack of a clear transition zone of low radar reflectivity in such simulations is another problem (Fovell and Ogura 1988). Recently, Morrison et al. (2009) demonstrated that a wide trailing stratiform region can be produced by adopting DM MP schemes. Given that mature squall lines contain distinct regions of precipitation of different characteristics that have been historically difficult to simulate, squall lines are good choices for testing and evaluating microphysics initialization and related predictions.

The rest of this paper is organized as follows. The cloud analysis system and new reflectivity equations are introduced in section 2. In section 3, the case to be simulated is introduced. Section 4 describes the setup of numerical experiments and the verification methods. Section 5 presents the results of experiments and section 6 gives a summary and conclusions.

2. The ARPS cloud analysis framework and enhancements

a. The ARPS cloud analysis framework

The ARPS system is used for the analysis and prediction of convective storms in this study. For the radar data, radial velocity is directly assimilated using the ARPS 3DVAR (Gao et al. 2004). The direct variational analysis of reflectivity in a 3DVAR framework is difficult because reflectivity is the function of several precipitation hydrometeors, and 3DVAR itself does not

know how to properly attribute observed reflectivity among hydrometeor species. Gao and Stensrud (2012) partially address this problem by restricting ice (rainwater) hydrometeors to above (below) the frozen level within the reflectivity formula, which is only an approximation. The method does not allow for the direct estimation of temperature, moisture, and cloud species either. Thus, a semiempirical complex cloud analysis is desirable and within the ARPS 3DVAR framework, it is used as an additional step after the 3DVAR analysis of radial velocity and other observations. The 3DVAR analysis effectively provides a background for the cloud analysis. The dominant precipitation type (rain, snow, freezing rain, or hail) is identified according to the background states and observed reflectivity before applying reflectivity formulas to retrieve mixing ratios at each grid point.

A brief description of the procedure diagnosing the precipitation types within the ARPS cloud analysis is given here. Precipitate begins as snow if the echo top is above the 0°C level; it is otherwise classified as rain. The precipitation type is then identified from echo top down to the bottom of each vertical grid column. If the ambient wet-bulb temperature is larger than 1.3°C, precipitate melts into rain. If the precipitate once again falls into an air layer colder than 0°C, it turns into freezing rain. A simple threshold of reflectivity above 45 dBZ is used to diagnose hail. More details can be found in Albers et al. (1996). To include graupel in this procedure, an approach similar to the simplified HID diagram of Lerach et al. (2010) is adopted in our study. The original ARPS cloud analysis is done first. After then, graupel is identified at a grid point when one of the following criteria is met: (i) the precipitation type is preidentified as snow, the reflectivity is between 32 and 41 dBZ, and the ambient temperature is below 0°C; (ii) the precipitation type is preidentified as freezing rain, the reflectivity is between 41 and 54 dBZ, and the ambient temperature is below 0°C; or (iii) the precipitation type is preidentified as hail, the reflectivity is between 41 and 54 dBZ, and the ambient temperature is below 0°C. Accordingly, the reflectivity threshold to be used to identify hail is now set to 54 dBZ instead of 45 dBZ. Wet and dry graupels are not distinguished and are assumed dry within the reflectivity formula following Milbrandt and Yau (2005a,b). The reflectivity formula for graupel in SMO is assumed to be the same as that for hail as shown in Table 1, but with different particle densities (913 kg m^{-3} for hail and 400 kg m^{-3} for graupel). Only one dominant type of hydrometeor is analyzed at any one model grid point, which is a limitation of the cloud analysis scheme. The model usually goes through a short period of adjustment

TABLE 1. Reflectivity equations in cloud analysis.

Hydrometer	Rain	Snow	Hail	Graupel
SMO	$q_r = \left(\dfrac{Z_{er} \pi^{1.75} N_{0r}^{0.75} \rho_r^{1.75}}{10^{18} \times 720 \rho^{1.75}} \right)^{4/7}$	Dry snow: $q_s = \left(\dfrac{Z_{es} \pi^{1.75} K_i^2 N_{0s}^{0.75} \rho_i^2}{10^{18} \times 720 K_i^2 \rho_s^{1.75} \rho^{0.25}} \right)^{4/7}$ Wet snow: $q_s = \left(\dfrac{Z_{es} \pi^{1.75} N_{0s}^{0.75} \rho_s^{1.75}}{10^{18} \times 720 \rho^{1.75}} \right)^{4/7}$	$q_h = \left[\dfrac{Z_{eh}}{\rho^{1.6625}} \left(\dfrac{\pi^{1.75} N_{0h}^{0.75} \rho_h^{1.75}}{10^{18} \times 720} \right)^{0.95} \right]^{0.6163}$	$q_g = \left[\dfrac{Z_{eg}}{\rho^{1.6625}} \left(\dfrac{\pi^{1.75} N_{0g}^{0.75} \rho_g^{1.75}}{10^{18} \times 720} \right)^{0.95} \right]^{0.6163}$
N0C	$q_x = \left[\dfrac{\|K\|_{lw}^2}{\|K\|^2} \dfrac{c_r^2}{G(\alpha_x)\rho^2} \right]^{(1+\alpha_x+d_x)/(1+\alpha_x+2d_x)} \left[N_{0x}\Gamma(1+\alpha_x) \right]^{d_x/(1+\alpha_x+2d_x)} \left[\dfrac{\Gamma(1+\alpha_x)}{\Gamma(1+\alpha_x+d_x)} \dfrac{\rho}{c_x} \right]^{(1+\alpha_x)/(1+\alpha_x+2d_x)} Z_{ex}^{(1+\alpha_x+d_x)/(1+\alpha_x+2d_x)}$			
N0D	$q_x = \left[\dfrac{\|K\|_{lw}^2}{\|K\|^2} \dfrac{c_r^2}{G_{(\alpha_x)}\rho^2} \right]^{(1+\alpha_x+d_x)/(1+\alpha_x+2d_x-c_{2x}d_x)} \left[c_{1x}\Gamma(1+\alpha_x) \right]^{d_x/(1+\alpha_x+2d_x-c_{2x}d_x)} (1000\rho)^{(c_{2x}d_x)/(1+\alpha_x+2d_x-c_{2x}d_x)} \left[\dfrac{\Gamma(1+\alpha_x)}{\Gamma(1+\alpha_x+d_x)} \dfrac{\rho}{c_x} \right]^{(1+\alpha_x)/(1+\alpha_x+2d_x-c_{2x}d_x)} Z_{ex}^{(1+\alpha_x+d_x)/(1+\alpha_x+2d_x-c_{2x}d_x)}$			

during the forecast. To be able to analyze coexisting species, more information is needed, either from observations or from a numerical model or both. For example, when an ensemble Kalman filter is used, multiple species can be analyzed making use of cross-covariance information derived from the background ensemble (Tong and Xue 2005).

To avoid adding too much hydrometeor content, an upper limit ($0.01\,\mathrm{kg\,kg^{-1}}$) is set to each hydrometeor. The hydrometeor fields are then horizontally smoothed to mitigate sharp gradients. For these reasons, the analyzed reflectivity field does not exactly match observed values at individual grid points but the differences are generally small. The original KRY equations were derived based on cloud physics and hydrometeor backscattering models while the SMO were derived based on curve and parameter fitting to observations. In both cases, N_{0x} is assume to be constant, and cannot vary temporally or spatially.

Under the assumption that observed reflectivity is much more reliable than its model counterpart is, the cloud analysis system replaces the background hydrometeors with those retrieved from observations. This also helps remove spurious precipitation found in the background. Important adjustments to temperature and moisture inside clouds are usually made by assuming a modified moist-adiabatic ascent of air parcels within the cloud that also accounts for environmental air entrainment as presented by Hu et al. (2006a). Schenkman et al. (2011) found that repeated adjustments of cloud water and water vapor mixing ratios in high-frequency assimilation cycles led to unrealistic warming in the middle troposphere in their mesoscale convective system (MCS) case. Guided by their study, during the cloud analysis steps of our test case, the cloud water and water vapor fields are not adjusted at all, only the precipitation hydrometeor mixing ratios (rain, snow, graupel, and hail) and in-cloud temperature are adjusted.

b. Cloud analysis based on diagnostic interception relations for two-moment microphysics initialization

As indicated earlier, we introduce new reflectivity equations based on the diagnostic $N_{0x} - W_x$ relationships and the gamma distribution. First, the PSD for each hydrometeor category is described by the analytical generalized gamma distribution function (Milbrandt and Yau 2005a), as given in (1). Although in the experiments to be presented in this paper the shape parameter α_x is set to zero, the complete generalized gamma distribution is used here for our method description (Ferrier 1994; Milbrandt and Yau 2005a):

$$N_{0x} = N_{Tx}\frac{1}{\Gamma(1+\alpha_x)}\lambda_x^{1+\alpha_x}, \tag{4}$$

$$\lambda_x = \left[\frac{\Gamma(1+d_x+\alpha_x)}{\Gamma(1+\alpha_x)}\frac{c_x N_{Tx}}{\rho q_x}\right]^{1/d_x}, \tag{5}$$

where N_{Tx} is the total number concentration for category x, and Γ is the gamma function. The variable ρ is the air density, c_x is a constant for each category and defined as $c_x = (\pi/6)\rho_x$, ρ_x is the density of each hydrometeor category, and the hydrometeor mass m_x is related to its diameter D_x by $m_x(D_x) = c_x D_x^{d_x}$. For spherical particles, d_x is 3. Here N_{Tx} can be derived from (4) and (5):

$$N_{Tx} = [N_{0x}\Gamma(1+\alpha_x)]^{d_x/(1+d_x+\alpha_x)}$$
$$\times \left[\frac{\Gamma(1+\alpha_x)}{\Gamma(1+d_x+\alpha_x)}\frac{\rho q_x}{c_x}\right]^{(1+\alpha_x)/(1+d_x+\alpha_x)}. \tag{6}$$

The sixth moment $M_x(6)$ of the PSD or the radar reflectivity factor Z_x is

$$Z_x = M_x(6) = \frac{G(\alpha_x)}{c_x^2}\frac{(\rho q_x)^2}{N_{Tx}}. \tag{7}$$

Using Rayleigh theory, Z_x can also be converted to the equivalent radar reflectivity Z_{ex} using

$$Z_{ex} = \frac{|K|_x^2}{|K|_w^2}\left(\frac{c_x}{c_r}\right)^2 Z_x, \tag{8}$$

where $|K|_x^2$ is the dielectric constant for the hydrometeor considered, taking a value of 0.176 for ice-phase hydrometeors (snow, hail, and graupel) and 0.93 for rain; $|K|_w^2$ is the dielectric constant for rain and takes a value of 0.93. Combining (6), (7), and (8), we can get the relationship between equivalent radar reflectivity and the mixing ratio of each category:

$$q_x = \left[\frac{|K|_w^2}{|K|_x^2}\frac{c_r^2}{G(\alpha_x)\rho^2}\right]^{(1+\alpha_x+d_x)/(1+\alpha_x+2d_x)}[N_{0x}\Gamma(1+\alpha_x)]^{d_x/(1+\alpha_x+2d_x)}\left[\frac{\Gamma(1+\alpha_x)}{\Gamma(1+\alpha_x+d_x)}\frac{\rho}{c_x}\right]^{(1+\alpha_x)/(1+\alpha_x+2d_x)}Z_{ex}^{(1+\alpha_x+d_x)/(1+\alpha_x+2d_x)}, \tag{9}$$

where

$$G(\alpha_x) = \frac{(6 + \alpha_x)(5 + \alpha_x)(4 + \alpha_x)}{(3 + \alpha_x)(2 + \alpha_x)(1 + \alpha_x)}. \tag{10}$$

Equation (9) based on a fixed intercept parameter is good for a pure SM scheme. Combined with (6), this set of equations using fix intercept parameter is labeled N0C (C indicates constant N0). By adopting a diagnostic relation between the water content

and intercept parameter of exponential distribution, the pure SM scheme can be improved (W14). The diagnostic relation for each category can be expressed as

$$N_{0x} = c_{1x} W_x^{c_{2x}}, \tag{11}$$

where W_x is related to mixing ratio q_x via $W_x = 1000\rho q_x$ (W_x is in $g\,m^{-3}$ and q_x is in $kg\,kg^{-1}$). Using (11), (9) becomes

$$q_x = \left[\frac{|K|_w^2}{|K|_x^2} \frac{c_r^2}{G(\alpha_x)\rho^2}\right]^{(1+\alpha_x+d_x)/(1+\alpha_x+2d_x-c_{2x}d_x)} [c_{1x}\Gamma(1+\alpha_x)]^{d_x/(1+\alpha_x+2d_x-c_{2x}d_x)}(1000\rho)^{(c_2 d_x)/(1+\alpha_x+2d_x-c_{2x}d_x)}$$
$$\times \left[\frac{\Gamma(1+\alpha_x)}{\Gamma(1+\alpha_x+d_x)}\frac{\rho}{c_x}\right]^{(1+\alpha_x)/(1+\alpha_x+2d_x-c_{2x}d_x)} Z_{ex}^{(1+\alpha_x+d_x)/(1+\alpha_x+2d_x-c_{2x}d_x)}. \tag{12}$$

Combining (6) and (11), the total number concentration can be calculated as

$$N_{Tx} = [c_{1x}(1000\rho)^{c_{2x}}\Gamma(1+\alpha_x)]^{d_x/(1+d_x+\alpha_x)}$$
$$\times \left[\frac{\Gamma(1+\alpha_x)}{\Gamma(1+d_x+\alpha_x)}\frac{\rho}{c_x}\right]^{(1+\alpha_x)/(1+d_x+\alpha_x)} q_x^{(1+c_{x2}d_x+\alpha_x)/(1+d_x+\alpha_x)}. \tag{13}$$

The logarithmic reflectivity factor (referred to as reflectivity in most parts of this paper) (in dBZ) is given by

$$Z = 10\log_{10}\left(\frac{Z_e}{1\,mm^6\,m^{-3}}\right). \tag{14}$$

Equivalent radar reflectivity of rain, snow, hail, and graupel, Z_{er}, Z_{es}, Z_{eh}, and Z_{eg}, could be derived from (14) after the dominant precipitation type at each grid point is diagnosed. Equations (12) and (13) are directly implemented into the enhanced ARPS cloud analysis system. This set of equations using diagnostic relations is labeled N0D (D indicates diagnostic N0). Equation (6) is also used to retrieve the number concentrations for SMO. The impact of our enhanced scheme on the analysis and forecast is evaluated with a squall line that occurred in southern China during 23–24 April 2007.

3. The 23 April 2007 south China squall-line case

On 23 April 2007, a squall line occurred over southern China. The case, including the structures and evolution of the squall line, was documented in Pan et al. (2012), and represents one of the most intense and well-organized squall lines that occurred over China. The squall line

had a pronounced trailing stratiform precipitation region during its later life cycle. By 2200 UTC 23 April 2007, a squall line had formed near the border between Guangxi and Guangdong provinces of China (see Fig. 1). The squall line was oriented east–westward (Fig. 1a), and propagated rapidly toward south. At 2300 UTC, the primary convective line (L1) is clearly defined and has gained a slight bow shape (Fig. 1b). A second, shorter, convective line (L2) formed at the west end of L1 (Fig. 1b) and those two gradually merged into one connected line extending over 500 km in length (Fig. 1c). During the 4-h period from 2200 UTC 23 April to 0200 UTC 24 April 2007, the squall line gradually intensified to form a broader, stronger, and well-organized convective line (Figs. 1a–e). The convective region, stratiform region, and a transition zone of weak reflectivity in between are clearly evident from 2300 UTC and the stratiform region expanded in area over the time. It began dissipating at around 0300 UTC 24 April (Fig. 1f) and moved out to the sea at 0400 UTC (Fig. 1g). After 0400 UTC 24 April, most of the squall line moved out to sea and was out of radar coverage. Additional details on the structure and evolution of this event can be found in Pan et al. (2012). Meng et al. (2012) further examined reasons of the formation of the bow structure and the rear inflow.

4. Design of experiments

a. The model configuration

The ARPS model is used as the prediction model in this study. It is a three-dimensional nonhydrostatic, compressible atmospheric model (Xue et al. 2000, 2001, 2003). For all the experiments in this study, the model is configured as follows: MY DM MP scheme with an
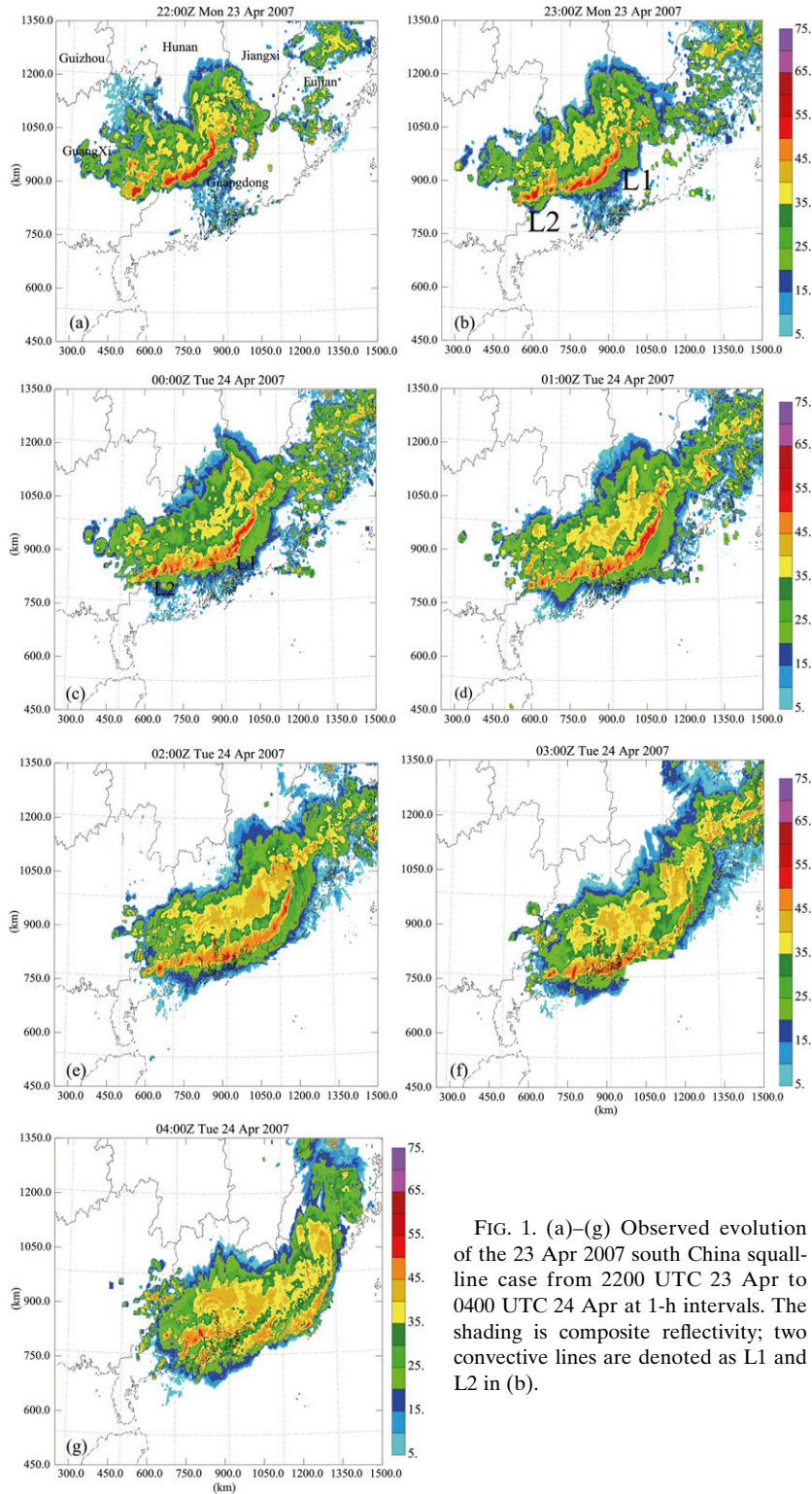
FIG. 1. (a)–(g) Observed evolution of the 23 Apr 2007 south China squall-line case from 2200 UTC 23 Apr to 0400 UTC 24 Apr at 1-h intervals. The shading is composite reflectivity; two convective lines are denoted as L1 and L2 in (b).
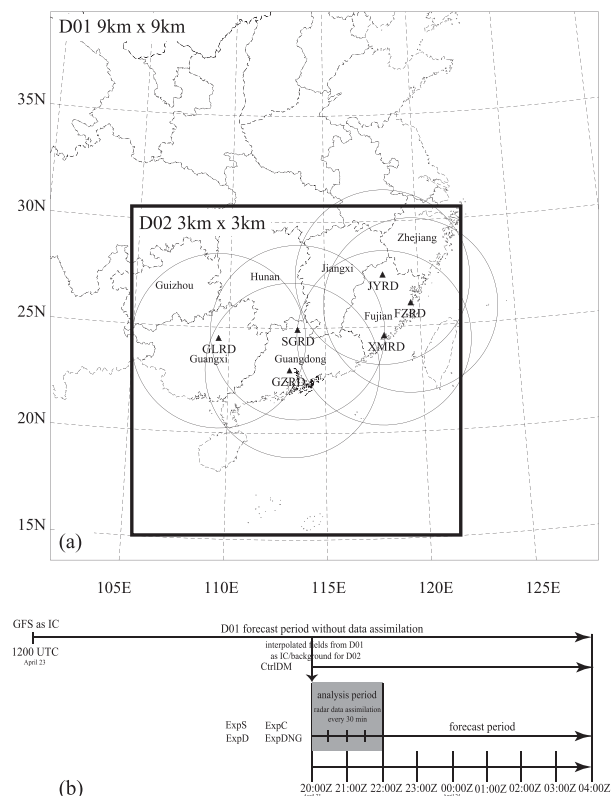
FIG. 2. (a) The nested domains of 9- and 3-km horizontal grid spacing and (b) the time lines of analyses and forecasts of experiments. The positions of radars are denoted by the ''up'' triangle in (a). The range circles of the Guilin radar (GLRD), Shaoguan radar (SGRD), Guangzhou radar (GZRD), Jianyang radar (JYRD), Fuzhou radar (FZRD), and Xia'men radar (XMRD) are for a maximum of 460 km.

assumption of $\alpha_x = 0$, fourth-order advection in both horizontal and vertical; a rigid top boundary combined with a wave absorbing layer; fourth-order computational filter; 1.5-order TKE-based subgrid-scale turbulent mixing scheme; and PBL parameterization. Surface fluxes were calculated using surface temperature and surface water content predicted by a two-layer land surface model, and radiative processes were calculated from Goddard Space Flight Center (GSFC) longwave and shortwave radiation parameterization. More details on the physics options can be found in the afore-referenced ARPS model description papers.

The experiments use two one-way nested domains with the Lambert conformal map projection. The outer domain consists of 323×323 horizontal grid points with a horizontal grid spacing of 9 km and covers the middle and southern parts of China (Fig. 2a). The inner domain consists of 579×579 horizontal grid points with a horizontal grid spacing of 3 km. The grid is stretched in the vertical, with 53 levels and a 400-m-average vertical spacing, and a near-surface vertical spacing of 50 m.

The outer domain was initialized from the National Centers for Environmental Prediction (NCEP) Global Forecast System (GFS) analysis at 1200 UTC 23 April 2007. Lateral boundary conditions from the GFS analyses were updated in 6-h intervals. Terrain data were derived from the 30-s global terrain data.

Level II data from six China New Generation Radar-1998 Doppler (CINRAD-98D) weather radars are used. They are radars at Guilin (GLRD), Shaoguan (SGRD), Guangzhou (GZRD), Jianyang (JYRD), Fuzhou (FZRD), and Xia'men (XMRD) (Fig. 2a). Both radial velocity and reflectivity data are assimilated, and are manually quality controlled before assimilation using the SOLO-II software (including velocity dealiasing and ground clutter removal) from NCAR.

b. Experiment design and verification methods

The analysis and forecast timelines of all experiments are shown in Fig. 2b. The 16-h, 9-km forecasts using MY DM MP scheme started from 1200 UTC 23 April 2004 using the GFS analyses as the initial and boundary conditions.

The $N_{0x} - W_x$ relations derived by W14 are based on a numerical simulation of a supercell storm typically at the U.S. central Great Plains environment. It is not necessarily suitable for subtropical squall lines in southern China. In this study, we follow the procedure proposed of W14 to derive our own version of the $N_{0x} - W_x$ relations. Specifically, a 3-km simulation of the squall line was performed using the MY DM scheme, starting from the initial condition interpolated from the 9-km simulation at 2000 UTC without radar data assimilation (CtrlDM). The outputs from the simulation were used to derive the relations, which will be given in the results section.

To investigate the impact of reflectivity equations within the cloud analysis, cycled 3-km data assimilation experiments are conducted. These experiments, named ExpS, ExpC, ExpD, and ExpDNG (Fig. 2b and Table 2), start from 2000 UTC and assimilate radar data every 30 min for 2 h until 2200 UTC, and are based on the SMO, N0C, and N0D equations in the cloud analysis. The mixing ratios and total number concentrations of rain, snow, graupel, and hail are calculated in the cloud analysis procedure for all these experiments. The background at 2000 UTC is interpolated from the 9-km valid forecasts at the same time. Forecasts are launched from the analyses at 2200 UTC and run through 0400 UTC 24 April. The MY DM scheme is used in those and all other experiments during the forecast. An additional experiment, ExpDNG, using the same configuration of ExpD but without the graupel class in the cloud analysis, is run to investigate the impact of adding the graupel category in the cloud analysis. When the cloud analysis system replaces the background hydrometeors

TABLE 2. List of 3-km experiments.

Expt	Reflectivity equation	Radar data assimilation window
CtrlDM	—	—
ExpS	SMO	2000–2200 UTC every 30 min
ExpC	N0C	2000–2200 UTC every 30 min
ExpD	N0D	2000–2200 UTC every 30 min
ExpDNG	N0D (without graupel)	2000–2200 UTC every 30 min

TABLE 3. Intercept parameter and density of each species for SMO and N0C.

Species	Intercept parameter (m^{-4})	Density ($kg\,m^{-3}$)
Rain	8.6×10^6	1000
Snow	3.8×10^6	100
Graupel	8.6×10^5	400
Hail	8.0×10^4	913

with those retrieved from observations, all hydrometeors are assumed to be zero first. In ExpDNG, graupel is zero in the cloud analysis but can form during the forecast. The intercept parameters and densities of each species for SMO and N0C are listed in Table 3. These fixed intercept parameters are set according to Xu (1983), which are based on several field observation projects in China.

The equitable threat scores (ETSs) and bias (BIASs) are used to evaluate the forecast performance of different experiments. The scores are calculated for composite reflectivity and 1-h accumulated precipitation and referred to as the reflectivity or precipitation ETSs/BIASs. The reflectivity scores are computed in the model grid space while the precipitation scores are computed in the observation space. The precipitation data are from rain gauge measurements.

The simulated reflectivity for verification (including the plots and the quantitative scores) uses the MY DM formula in this paper, matching the MP scheme of the forecasts even though the intercept parameter is fixed within SMO and N0C scheme. The different reflectivity formula used in the cloud analysis and the plotting program can create differences between the analyzed and observed reflectivity at the analysis time. After the cloud analysis, a nine-point horizontal smoother is applied to the analyzed hydrometeor fields to avoid sharp gradients. (Reflectivity is not calculated when the mixing ratio is less than $10^{-18}\,kg\,kg^{-1}$ or the number concentration is less than $10^{-5}\,m^{-3}$).

5. Results and discussion

a. The diagnostic $N_{0x} - W_x$ relations

As stated earlier, our $N_{0x} - W_x$ relations are derived from the output of experiment CtrlDM. After 7 h of forecast at 0300 UTC, the squall-line system is mature and well developed (not shown). Between 0300 and 0400 UTC, the zeroth and third moments of rain, snow, graupel, and hail are output every 10 min. Power-law relations between intercept parameter and hydrometeor content, $N_{0x} = c_1 W_x^{c_2}$, are derived from these output using a least squares fitting between the logarithm of N_{0x} and W_x following W14. Figure 3 shows the scatterplots

of N_{0x} versus W_x and the fitted relations between them; the slope of the dashed lines defines the exponent of the power-law relation for each species. The coefficients of determination (R^2) for rain, snow, graupel, and hail are 0.11, 0.07, 0.44, and 0.11, respectively. For rain, Fig. 3a suggests that the new relation is fitting data points spanning both convective and stratiform rain; convective rain is characterized by small N_{0r} and large W_r while stratiform rain has larger N_{0r} and smaller W_r. While there are still quite a lot of scatter around the fitted relations, the diagnostic relations represent improvements over the fixed intercept parameters in this squall-line case. The rainwater content and number concentration in a vertical slice across the forecast squall line at 0200 UTC of CtrlDM (Fig. 4a) are shown in Fig. 4b. It can be noted that in the leading convective region (near 250 km in the horizontal axis), the water content is high ($>1\,g\,m^{-3}$) but the number concentration is relatively low, indicating the presence of large raindrops. Behind the convection region at a 3–4-km height level is a region of moderate rainwater content (less than $1\,g\,m^{-3}$), but with the highest values of number concentration, corresponding to the stratiform precipitation region. The fitted line also indicates that there is a strong dependence of the intercept parameter on water content, and there is a three-order-of-magnitude change in the value of N_{0r} based on the fitting. Apparently, fixed N_{0r} is not very appropriate. For squall lines that contain both extensive convective and stratiform precipitation regions, this seems especially important, and perhaps more so than supercell storms that tend to be dominated by convective precipitation. Significant slopes are also found for graupel, hail, and somewhat less for snow according to Fig. 3. The fitted power-law relations are listed in Table 4, and these relations are applied to (12) and (13) within our cloud analysis system to obtain the analyses of mixing ratios and total number concentrations from the reflectivity component attributed to the respective species.

b. Final analyses from cycled data assimilation experiments

As mentioned earlier, the cloud analysis system places its trust on the radar observations; therefore, it replaces
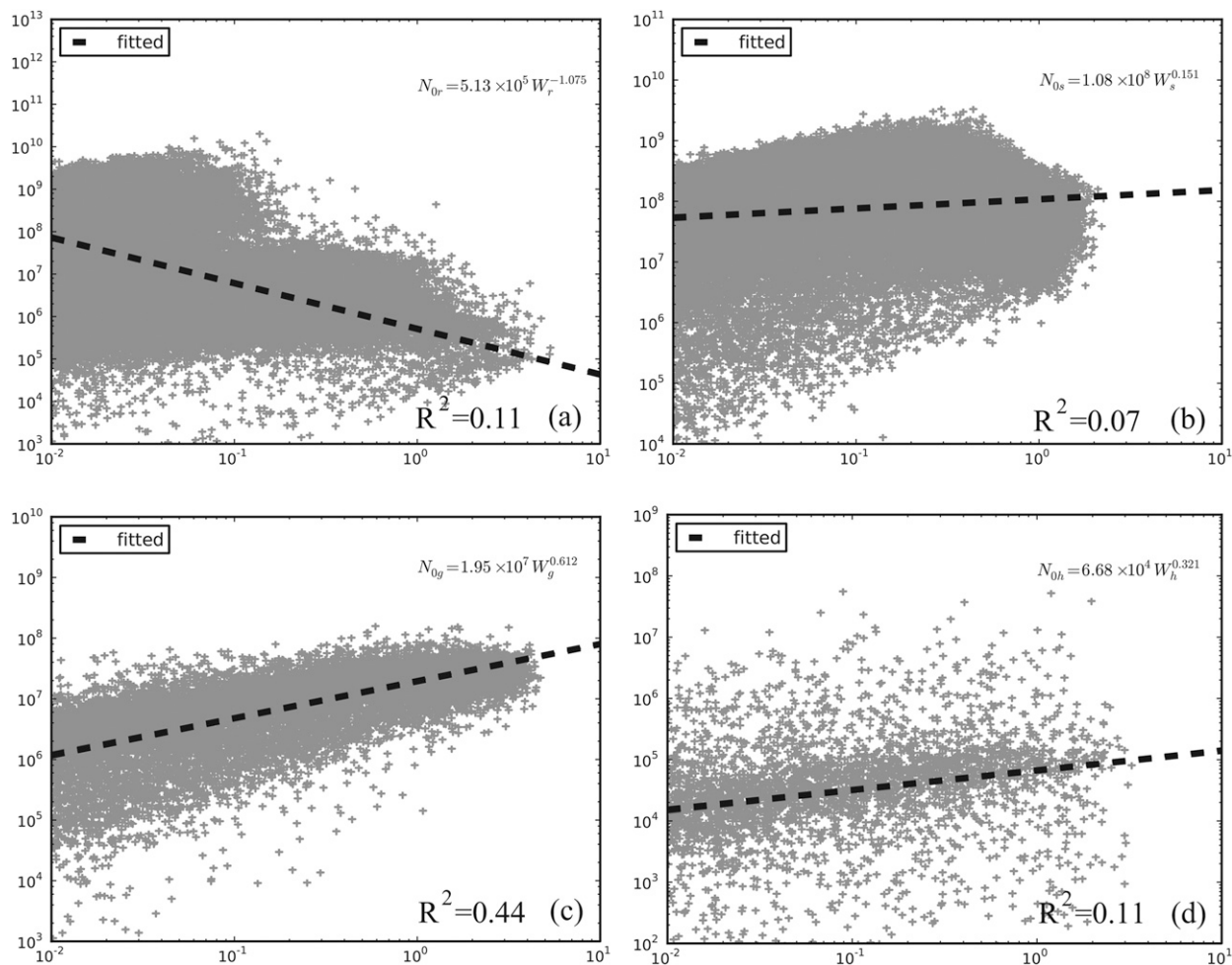
FIG. 3. Scatterplots and fit of (a) rain intercept parameter N_{0r}, (b) snow intercept parameter N_{0s}, (c) graupel intercept parameter N_{0g}, and (d) hail intercept parameter N_{0h} vs corresponding water/ice content W_x from CtrlDM. One data point out of every 100 is plotted in the scatterplots. The bold dashed lines show the fitted relation; the slope of the line defines the exponent of the power-law relation. The coefficient of determination (R^2) for each species is indicated in each panel.

the hydrometeors found in the background with those retrieved from observations. Because of the dependency of the precipitation-type classification on the background temperature, there will be differences among the analyzed hydrometeor fields due to the background differences but the differences are relatively small. The results from the final analyses of the experiments that assimilate radar data every 30 min starting at 2000 through 2200 UTC are presented in this section to show the effects of the enhanced cloud analysis on the analysis.

Figure 5 presents the analyzed composite reflectivity and the wind vectors at 2200 UTC. The wind in front of the squall line is mainly westerly but shifts to northwesterly behind the squall line. It should be noted that the reflectivity differences are caused by different reflectivity formulas in the analysis and plotting steps. As pointed out earlier, for the graphic plotting, the reflectivity

formula corresponding to the DM MP scheme is used to calculate the analyzed reflectivity; which may be different from the observed reflectivity used in the cloud analysis. In a sense, the plotted reflectivity represents the reflectivity expected from the model state assuming the DSD is what would be given by the DM MP scheme used by the prediction model. The composite reflectivity analyzed by ExpC, ExpD, and ExpDNG (Figs. 5b–d) is close to the observed values (Fig. 1a). For ExpS, the composite reflectivity above 50 dBZ is underestimated.

Figure 6 shows the reflectivity bias score (shaded) from the surface to 10 km MSL at 2200 UTC for reflectivity thresholds between 15 and 50 dBZ overlaid with ETS scores. Bias score is above or below 1, when the analyzed reflectivity is higher or lower than the observation. ExpS (Fig. 6a) underestimates reflectivity at
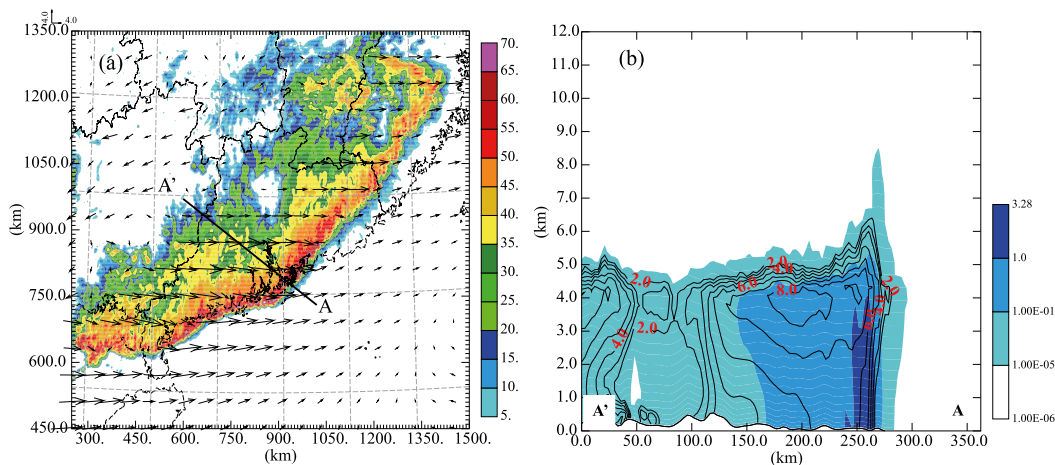
FIG. 4. (a) Composite reflectivity and wind vectors at 1 km MSL at 0200 UTC 24 Apr 2007 from CtrlDM, and (b) vertical cross section of rainwater content (g m^{-3}) (color shaded) and the logarithm of rainwater number concentration (contours) along A–A′ in (a).

all thresholds above 4.5 km MSL. In ExpC, ExpD, and ExpDNG (Figs. 6b–d), the underestimation are greatly reduced. Major bias only exists at a threshold above 40 dBZ and above 4.5 km MSL.

The reflectivity underestimation in ExpS (Fig. 6a) are caused by the inconsistency in reflectivity formulas used in the analysis (using SMO equations) and the plotting (using MY DM equations) steps. To demonstrate this, we conduct a simple idealized test, which mimics the cloud analysis procedure. We calculated, using SMO, N0C, and N0D schemes, respectively, the mixing ratios and number concentrations from a given reflectivity (treated as an "observation"). After obtaining the "analyzed" mixing ratios and number concentrations, we simulated analyzed reflectivity using the DM MY scheme. This process was done for all reflectivity between 15 and 65 dBZ with an interval of 1 dBZ. Air density is assumed to be 0.68 kg m^{-3}. The mixing ratio, number concentration, and the analyzed reflectivity are plotted against "observed" reflectivity and shown in Fig. 7. Figures 7a–c show the situation assuming the hydrometeor is rainwater. The rainwater mixing ratio and total number concentration from SMO and N0C are identical (Figs. 7a–c, green and blue lines). They are smaller than those from the N0D scheme (Fig. 7a, red line) for reflectivity below 25 dBZ and greater for reflectivity beyond 25 dBZ. The SMO, N0C, and N0D scheme all produce the same analyzed reflectivity. Figures 7d–f show the situation assuming the hydrometeor is in ice phase. For simplicity, in this idealized test, it is assumed that hail is identified when reflectivity is 54–65 dBZ, graupel is 32–54 dBZ, and snow is 15–32 dBZ. In SMO, the snow is considered dry snow when the temperature is less than 0°C and considered to be

wet snow when the temperature is between 0° and 5°C. For wet snow, a fraction of reflectivity factor of the snow (0.2$t_c Z_{es}$, t_c is the temperature in °C) is further treated as the reflectivity factor of rain. Both mixing ratios and number concentrations of dry (black dot line) and wet snow (green line) are calculated and plotted in Fig. 7. There is only one equation for snow in N0C and N0D; wet snow identification is not included. The mixing ratio and total number concentration of the dry snow from SMO are the same as those of N0C, but are lower than those of N0C for wet snow. The mixing ratios of wet snow, graupel, and hail from the SMO scheme are all smaller than those from the N0D scheme for all reflectivity thresholds. The number concentrations from the SMO scheme are also smaller than those from the N0D scheme. As a result, the analyzed reflectivity of wet snow, graupel, and hail from the SMO scheme are all smaller than those from the N0D scheme. When the mixing ratio and total number concentration are rather small, the analyzed reflectivity values could fall below zero. The cloud analysis system imposes a lower limit of zero analyzed reflectivity; the same limitation is used for Fig. 7. This leads to the zero analyzed reflectivity values between 15 and 25 dBZ of wet snow (Fig. 7f). To conclude, the reflectivity biases in ExpS

TABLE 4. The derived diagnostic relations for N_{0x}.

| Species	Diagnostic relation derived from CtrlDM simulation
Rain	$N_{0r} = 5.13 \times 10^5 W_r^{-1.075}$
Snow	$N_{0s} = 1.08 \times 10^8 W_s^{0.151}$
Graupel	$N_{0g} = 1.95 \times 10^7 W_g^{0.612}$
Hail	$N_{0h} = 6.68 \times 10^4 W_h^{0.321}$
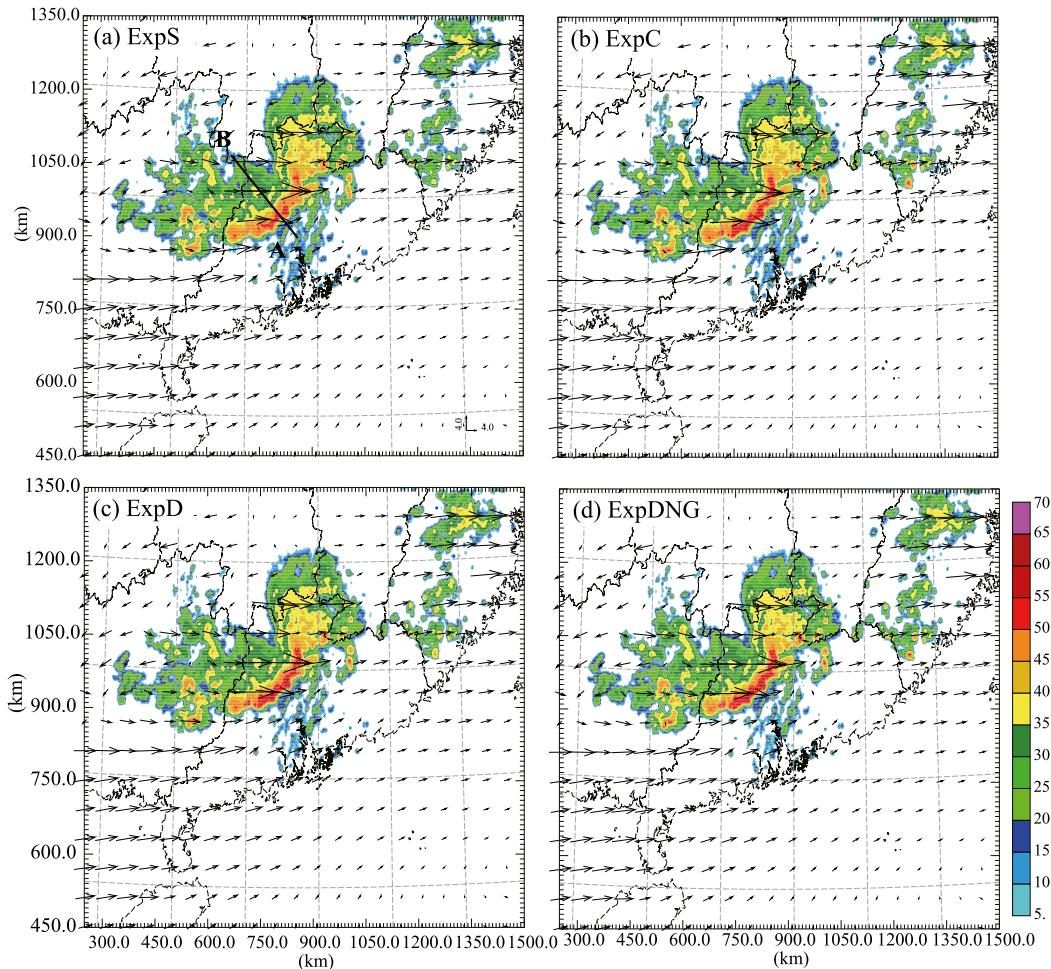
FIG. 5. Composite reflectivity and wind vectors at 1 km MSL at 2200 UTC 23 Apr 2007 from experiments (a) ExpS,
(b) ExpC, (c) ExpD, and (d) ExpDNG, respectively.

are produced mainly because we use one reflectivity
formula to retrieve mixing ratio while we use another
formula to simulate analyzed reflectivity from the re-
trieved variables.

The reflectivity biases in ExpC, ExpD, and ExpDNG
are evidently reduced since the same reflectivity equa-
tions are used in both the analysis and the plotting steps.
The residual biases are caused by two reasons. First, a
horizontally nine-point smoother is applied to the ana-
lyzed model variables before they are finalized; second,
there is an upper bound that limits the maximum hy-
drometeor mixing ratio obtained in the analysis. In an
additional experiment where the smoother and the limits
are removed, the reflectivity biases in ExpC, ExpD, and
ExpDNG disappear totally (figures not shown here). This
is confirmed in Fig. 7c. N0C and N0D schemes yield exact
45° slope lines in Fig. 7c. It means that in a situation
without the smoother and the limits, the analyzed re-
flectivity is exactly the same as the observed one.

To better understand the differences among the ana-
lyses using the SMO, N0C, and N0D equation sets, we
further compare the mixing ratios along line A–B in
Fig. 5a. In comparison with the hydrometeor fields from
ExpDNG, the areas with less snow and hail above the
freezing level in the convective region in ExpD corre-
spond to where graupel is analyzed based on the graupel
classification. If reflectivity is between 32 and 41 dBZ
and the ambient temperature is below 0°C, the hydro-
meteor would be identified as graupel in ExpD rather
than snow as in ExpDNG. If reflectivity falls between 41
and 54 dBZ and the ambient temperature is below 0°C,
graupel is identified in ExpD rather than hail as in
ExpDNG. Part of the hail in ExpDNG is identified as
rain in ExpD because the threshold of reflectivity to
diagnose hail is increased from 45 to 54 dBZ when using
graupel classification. Graupel exists in both the con-
vective and stratiform regions at heights above 4.0 km.
By using diagnostic relations, the mixing ratios of snow
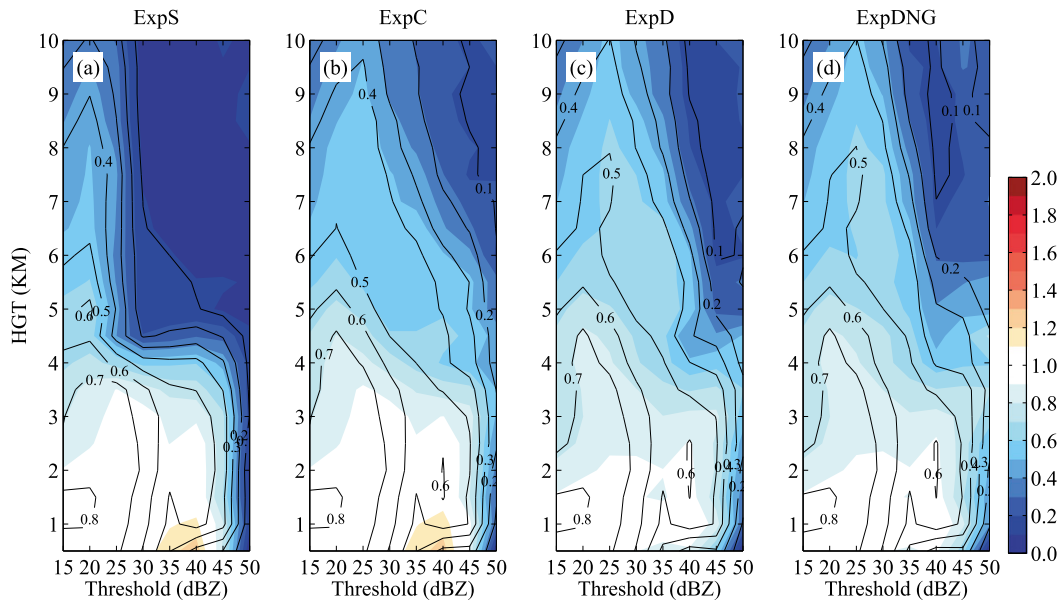
FIG. 6. Reflectivity ETS (contours) and bias scores (color shaded) as functions of height and for different thresholds valid at analysis time 2200 UTC 23 Apr 2007 from (a) ExpS, (b) ExpC, (c) ExpD, and (d) ExpDNG.

and graupel (Figs. 8g,k) are greater than those obtained with constant intercept parameters (Figs. 8f,j). The maximum of the logarithm of total number concentration is given in the figure for each hydrometeor. The maxima of number concentrations of snow, graupel, and hail from ExpD are also greater than those from ExpS and ExpC. With the wet snow classification within SMO scheme, the rain mixing ratio immediately below the freezing level is greater and snow mixing ratio is less than in N0C and N0D. Away from the freezing level, ExpS and ExpC have the same snow and rain mixing ratio. In general, the new reflectivity assimilation procedure produces better analyses of the hydrometeor mixing ratios and size distributions, which play an important role in the dynamics of the squall line. Previous studies (Gamache and Houze 1982; Houze and Churchill 1987; Szeto and Cho 1994a,b; Bryan and Morrison 2012) suggest that the trailing stratiform region is primarily composed of ice crystals and snow particles that are created by the rearward transportation of the ice particle from the convective region. Melting of the ice particles at the stratiform is important in driving the mesoscale downdraft and rear-to-front flow. The correct types of ice particles and their size distributions are important to produce proper structures of squall lines. The increased ice particle mass and numbers from ExpD seem to improve the squall-line prediction in the model.

c. Forecasts from cycled data assimilation experiments

In this section, we examine the forecasting results from experiments ExpS, ExpC, ExpD, and ExpDNG. From

final analyses at 2200 UTC, 6-h free forecasts are made. As mentioned earlier, although the cloud analysis system trusts the radar observations (it replaces the hydrometeors found in the background with those retrieved from observations), differences among the analyzed hydrometeor fields still exist due to the background temperature and water vapor differences. The difference in the resulting forecasts can however be much bigger due to the differences in the background and the accumulated effects of cloud analysis differences within the cycles. For these reasons, we will focus on the comparison of forecasts among these four cycled experiments.

The forecast composite reflectivity and the wind vectors at 0000 and 0200 UTC are plotted in Fig. 9. For the forecasts at 0000 UTC, small areas of stratiform precipitation behind the leading convective region of the squall line start to appear, as pointed to by the black arrow. By 0200 UTC, an elongated region of stratiform precipitation region has developed separated from the leading line of intense convection by a clearly defined transition zone of weaker precipitation. The stratiform precipitation region in ExpS (Fig. 9b) and ExpC (Fig. 9d) is much narrower than that from ExpD (Fig. 9f). In the region $x = 800–1100$ km and $y = 800–950$ km, ExpD shows evident stratiform precipitation while ExpS and ExpC totally miss this feature. Cross sections along line C–D in Fig. 9b of observed radar reflectivity and the four forecasts are shown in Fig. 10. The physical variables shown in Fig. 10 are averaged across a 18-km-wide band centering on line C–D to improve representativeness. In all four experiments, the cold pools as defined by the -3-K potential temperature perturbation
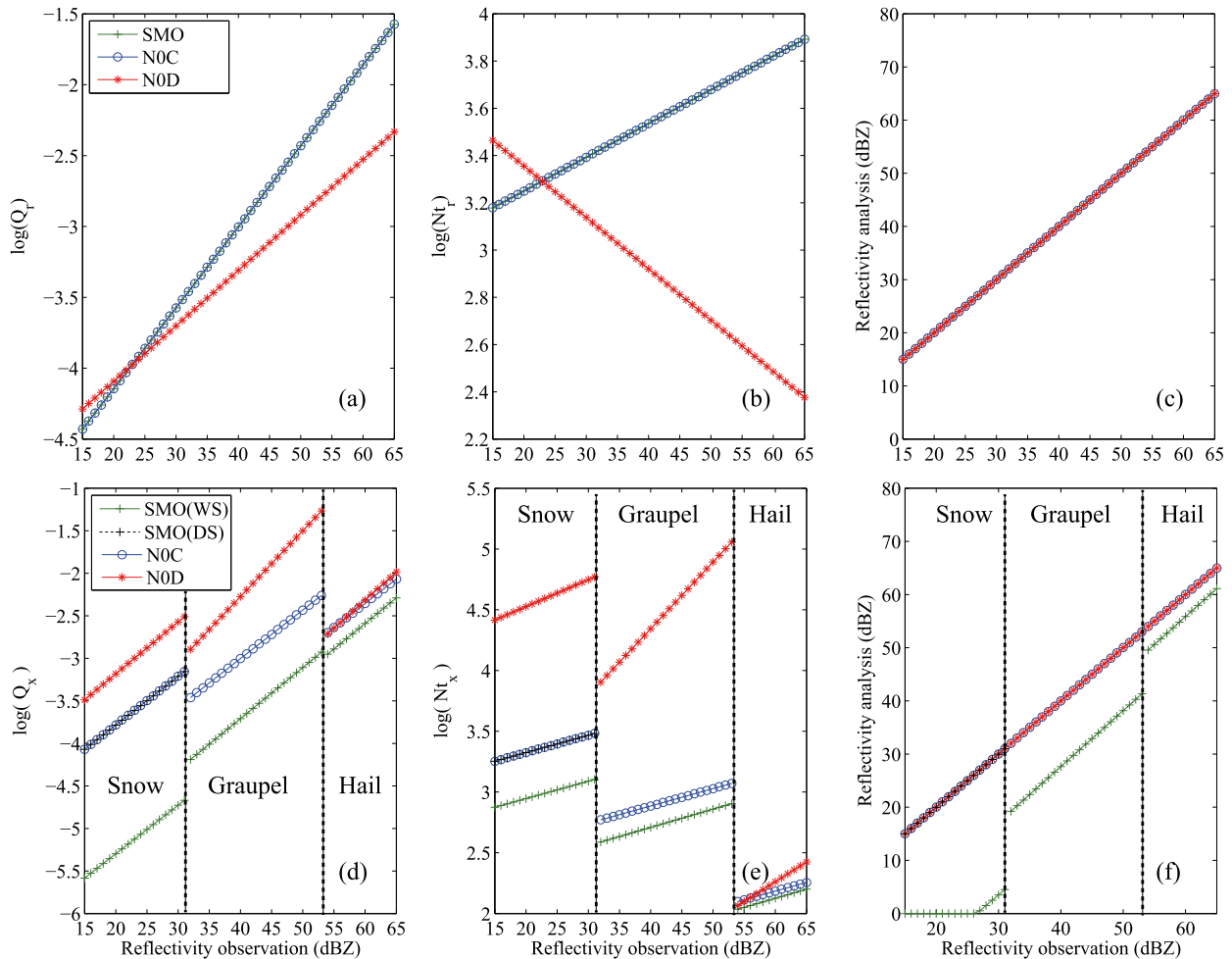
FIG. 7. The retrieved mixing ratios and number concentrations of (a),(b) rain and (d),(e) ice content using SMO, N0C, and N0D equation sets. (c),(f) The "analyzed" reflectivity calculated using the MY DM formulations from retrieved mixing ratios and number concentrations corresponding to the "observed" reflectivity in the horizontal axis.

(from the mean ahead of the squall line), its contour is about 3 km deep in the convective region. The ascending front-to-rear (FTR) flow above the cold pool transports the hydrometeors across the system from the leading-edge convective line to the trailing stratiform region, and rear inflow jet (RIJ) enters the squall line from the rear below 6 km and down into the convective region under 3 km. The RIJ from ExpD is slightly weaker than those from ExpS and ExpC in the region 50–150 km in the horizontal axis and 3–5 km in the vertical axis. ExpD predicts a well-defined convection region, a wide stratiform region, and a clear transition zone (Fig. 10d), and has a better agreement with radar observations. ExpS and ExpC do not show a separation between the stratiform and convective precipitation (Fig. 10b). Without graupel, the forecast from ExpDNG (Fig. 10e) is slightly worse than ExpD.

The ETS scores and frequency biases for predicted composite reflectivity at the 15-, 30-, and 45-dBZ thresholds,

chosen to roughly represent the entire, stratiform, and convective precipitation regions, respectively, are shown in Fig. 11. In general, ExpD and ExpDNG have very similar ETS scores throughout the 6-h forecast period at the 15- and 30-dBZ thresholds, and they are the highest for both thresholds (Figs. 11a,c) except for the final one hour for the 30-dBZ threshold (Fig. 11c). ExpS generally yields the lowest ETS scores for the 15- and 30-dBZ thresholds, but gives higher ETS scores at the final two hours at 45 dBZ (Fig. 11e). The frequency biases from ExpD and ExpDNG are closest to 1 at the 15-dBZ threshold. For the 30-dBZ threshold, the bias is closer to 1 for all experiments, with those of ExpD and ExpDNG having the smallest biases overall. ExpS is largely underestimated in the first three hours of the forecast (Fig. 11d). For the 45-dBZ threshold, there is a significant overestimation in all four experiments (Fig. 11f).
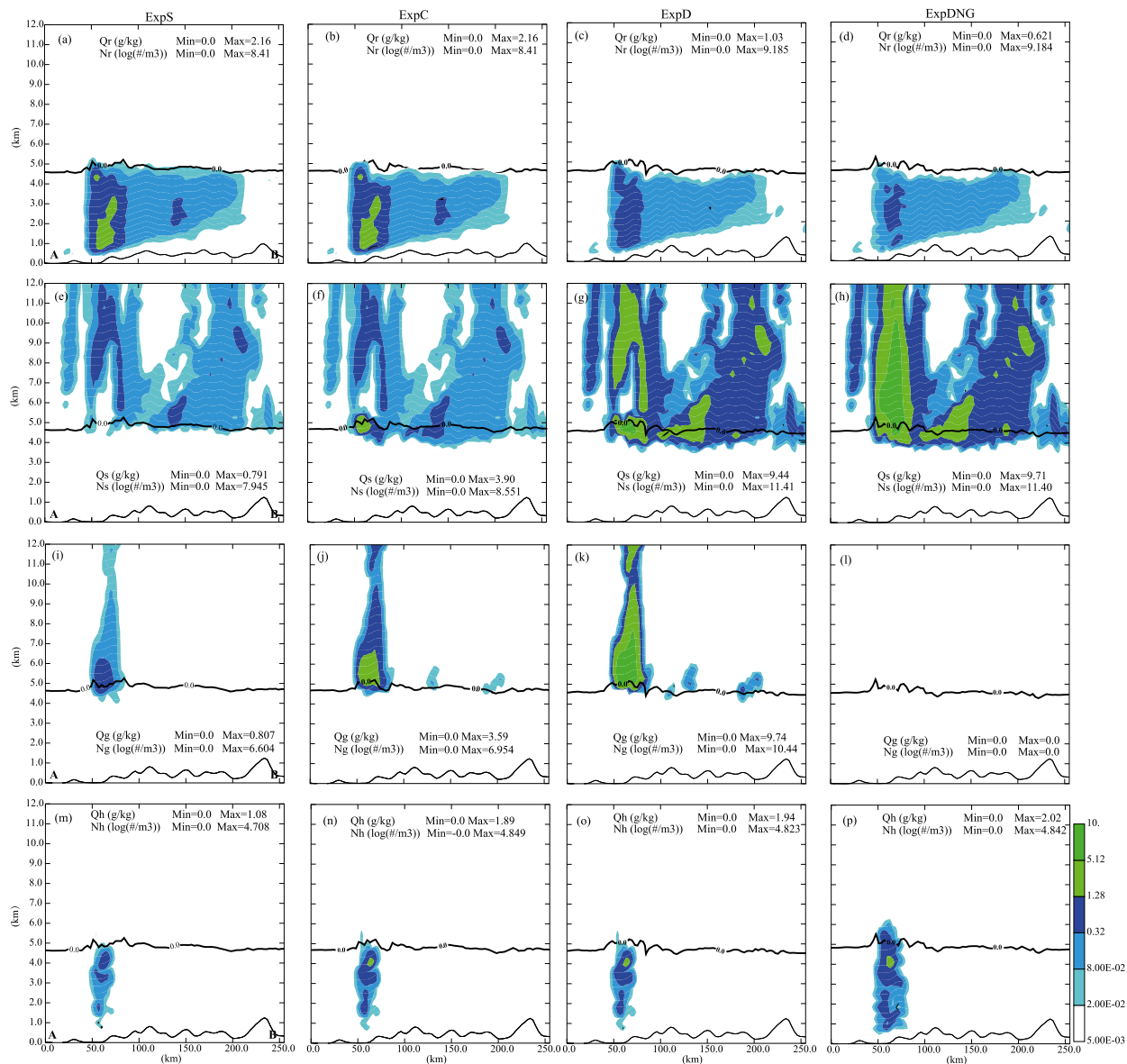
FIG. 8. Cross sections of (a)–(d) rain, (e)–(h) snow, (i)–(l) graupel, and (m)–(p) hail mixing ratios (color shaded) from ExpS, ExpC, ExpD, and ExpDNG along line A–B in Fig. 5a at 2200 UTC 23 Apr. Thick line is the freezing level. The maximum and minimum of mixing ratio and logarithm of number concentration are indicated.

We further compared the forecasts against 1-h accumulated precipitation at thresholds of 0.5, 6, and 10 mm h^{-1} (Fig. 12). More prominently than the reflectivity ETS scores, ExpD, ExpC, and ExpDNG clearly outperform the ExpS in terms of the precipitation ETS scores in the first 4 h of forecast, and are only passed by ExpS in the final two hours at the 6 and 10 mm h^{-1} threshold. The ETS scores of ExpD and ExpDNG are very similar for the two smaller thresholds (Figs. 12a,c), but the difference becomes clear for the 10 mm h^{-1} threshold (Fig. 12e), indicating that the analysis of the graupel category does improve the prediction of heavy rainfall. Bias scores of ExpS are

closest to 1.0 at threshold of 0.1 mm h^{-1}. Compared to ExpC and ExpS, the biases of ExpC and ExpD are comparable (Fig. 12d) at the 6 mm h^{-1} threshold, and close to 1. For the highest threshold, ExpD obtained the highest ETS scores and BIAS scores closest to 1. Overall, ExpD produces the best precipitation forecast among the four experiments.

Overall, when we assimilate radar data for 2 h with 30-min intervals using our enhanced cloud analysis scheme and combine it with prediction using a two-moment MP scheme, the stratiform region and transition zone in terms of the simulated reflectivity are
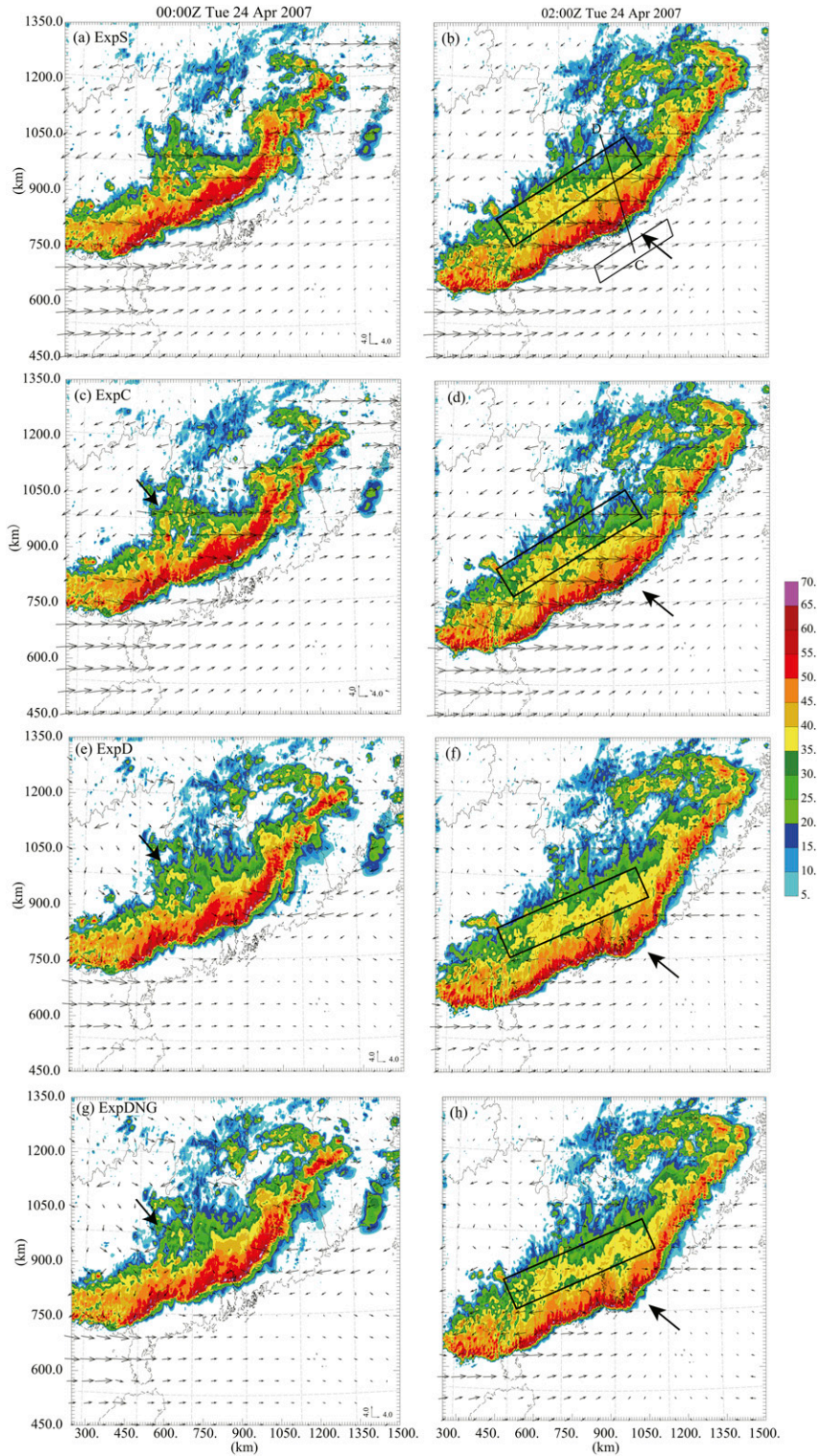
FIG. 9. Forecast composite reflectivity and wind vectors at 1 km MSL for (a),(b) ExpS; (c),(d) ExpC; (e),(f) ExpD; and (g),(h) ExpDNG at (left) 0000 UTC and (right) 0200 UTC 24 Apr 2007. The stratiform region is indicated by the box behind the convective region. The box in front of the system is used and explained in Fig. 10.
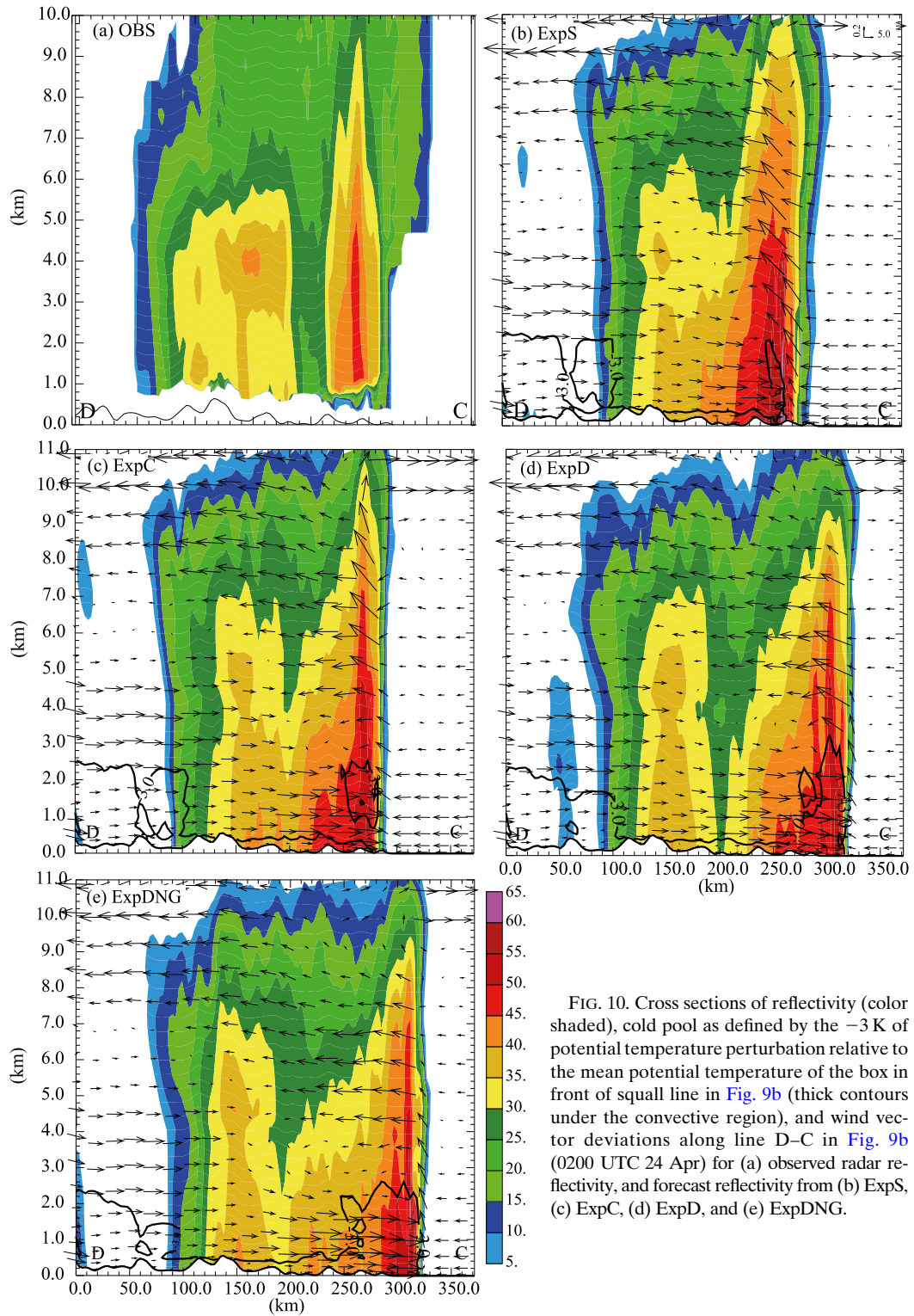
FIG. 10. Cross sections of reflectivity (color shaded), cold pool as defined by the −3 K of potential temperature perturbation relative to the mean potential temperature of the box in front of squall line in Fig. 9b (thick contours under the convective region), and wind vector deviations along line D–C in Fig. 9b (0200 UTC 24 Apr) for (a) observed radar reflectivity, and forecast reflectivity from (b) ExpS, (c) ExpC, (d) ExpD, and (e) ExpDNG.

better captured. Also, better precipitation forecast results are obtained when using the reflectivity equations based on diagnostic intercept parameters [compared to using the SMO reflectivity equations

(experiment ExpS)] and equations based on a fixed intercept parameter (experiment ExpC). The identification and analysis of the graupel category helps us to further improve heavier rainfall prediction. We see
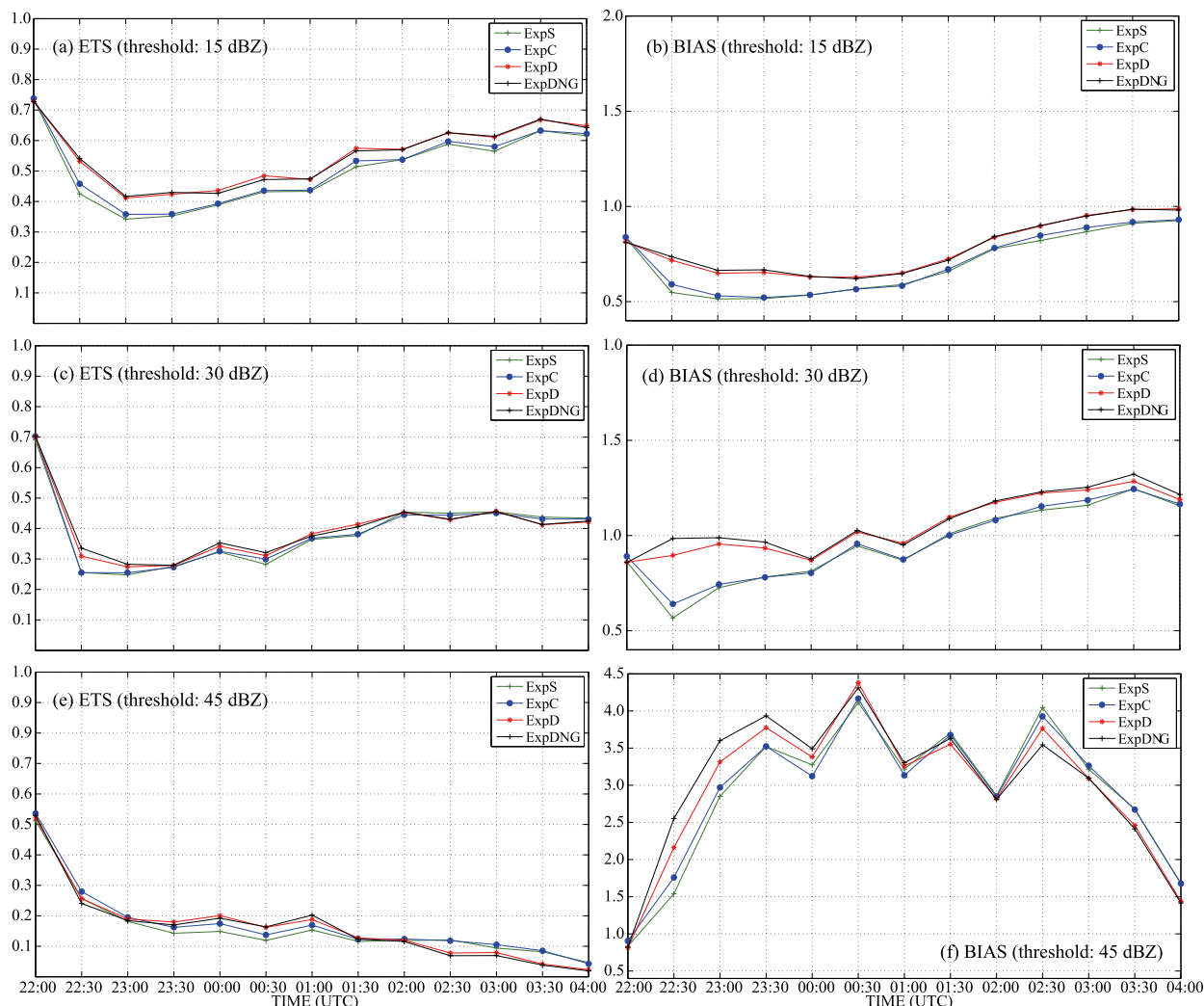
FIG. 11. (a),(c),(e) Equitable threat scores and (b),(d),(f) frequency biases of predicted composite reflectivity for 15-, 30-, and 45-dBZ thresholds from ExpS, ExpC, ExpD, and ExpDNG.

bigger separations in the ETS and bias scores of hourly precipitation than those of simulated reflectivity. We think the precipitation-based scores are more robust because the reflectivity calculation is strongly sensitive to the reflectivity formula used. Also, the hourly precipitation is accumulative while the reflectivity is instantaneous; the latter is more sensitive to timing and location errors in the forecast features.

6. Summary and conclusions

This study enhances the existing ARPS cloud analysis system for the assimilation of radar reflectivity data, so that it can be used to initialize, in cycled and noncycled modes, both mixing ratios and total number concentrations associated with a double-moment microphysics

scheme, which contains both graupel and hail categories. Toward this goal, the diagnostic intercept parameter approach is taken, where a diagnostic relation between the intercept parameter and the hydrometeor content, or $N_{0x} - W_x$, is derived for each hydrometeor category from model simulation output produced using a double-moment microphysics scheme. This approach is based on earlier studies that found strong relationships between the intercept parameters and corresponding hydrometeor contents, and the fact that a single-moment MP scheme using diagnosed intercept parameters could produce results similar to the corresponding double-moment scheme.

A new reflectivity equation set is derived based on the diagnostic relations derived and the gamma particle/drop size distributions. To be able to analyze both graupel and hail categories from reflectivity data, a graupel–hail
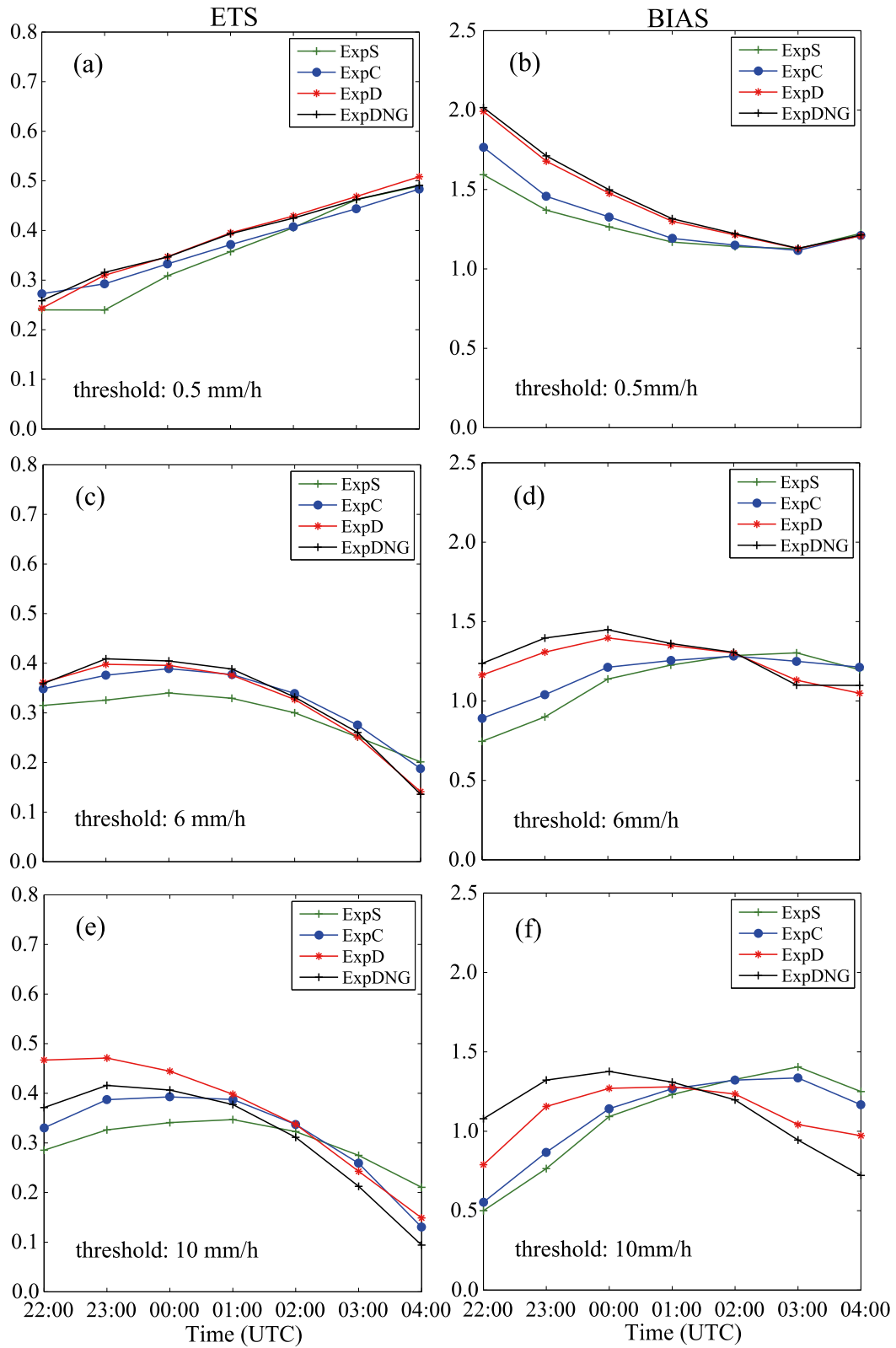
FIG. 12. Equitable threat scores and frequency biases of predicted hourly accumulated precipitation at (a),(b) 0.5; (c),(d) 6; and (e),(f) 10 mm h^{-1} thresholds for experiments ExpS, ExpC, ExpD, and ExpDNG.

classification algorithm is implemented in the cloud analysis system to determine the dominant hydrometeor category. A squall line that formed on 23–24 April 2007 over southern China that contained classical leading convective lines and the trailing stratiform precipitation regions is used to evaluate the impacts of the enhanced cloud analysis scheme on the analysis and prediction of the precipitation structures and the amount associated with the squall line. The $N_{0x} - W_x$ relations used were derived from a baseline double-moment simulation for the same case without radar data assimilation, following the procedure developed by W14.

To examine the impacts of the enhanced cloud analysis system on the analyses and subsequent forecasts, four experiments using different reflectivity equations, including the one based on the diagnostic intercept parameters, were carried out. Those experiments assimilated radar data over a 2-h period at 30-min intervals.

The new reflectivity equation set based on diagnosed intercept parameters improves the stratiform reflectivity compared to radar observations than the original reflectivity equations using the fix intercept parameters. For initializing the MY DM PM scheme, the new reflectivity equation set provides the DSDs expected from the DM MP scheme used by prediction model, which could produce the reflectivity close to observation. The forecasts using the enhanced cloud analysis capture wider stratiform regions and a more distinct transition zone from the leading convective line. The short-term precipitation forecasting skill is also improved. Additional experiments without including the graupel category in the analysis are conducted to show the effects of adding graupel; the hourly precipitation skill scores were improved for a higher precipitation threshold ($>10\,\mathrm{mm\,h^{-1}}$) when the graupel category is included.

In this study, we derived the diagnostic intercept parameter relations based on a base-line simulation of the same case with the same DM microphysics scheme used for the data assimilation and prediction experiments. The rationale for doing this is that to obtain reflectivity equations and a cloud analysis scheme that are as consistent with the DM scheme to be used as possible, given the limited observational information (from radar the radial velocity and reflectivity only). In a sense, this is similar to the ensemble Kalman filter (e.g., Tong and Xue 2005; Xue et al. 2010) where correlation relations among different model state variables, including those among total number concentrations and mixing ratios, are derived from an ensemble of predictions using the same model. When the number of observed parameters is much smaller than the number of state variables to be initialized, additional assumptions, physical constraints, and/or information from a prediction model, have to be utilized to overcome the underdeterminedness problem. For this study, we solve this problem by utilizing diagnostic intercept parameter relations and hydrometeor identification algorithms within a semiempirical cloud analysis system. This paper serves as a proof of concept for this approach while the generality of the results and conclusions require further testing with more cases (e.g., severe convective storms, winter storms, and stratiform precipitation) and over different regions. The variability of the derived relations across different cases and how much the relationships depend on the specific microphysics schemes used, also requires further investigation.

REFERENCES

Albers, S. C., J. A. McGinley, D. A. Birkenheuer, and J. R. Smart, 1996: The Local Analysis and Prediction System (LAPS): Analysis of clouds, precipitation and temperature. *Wea. Forecasting*, **11**, 273–287, doi:10.1175/1520-0434(1996)011<0273:TLAAPS>2.0.CO;2.

Biggerstaff, M. I., and R. A. Houze Jr., 1991: Midlevel vorticity structure of the 10–11 June 1985 squall line. *Mon. Wea. Rev.*, **119**, 3066–3079, doi:10.1175/1520-0493(1991)119<3066:MVSOTJ>2.0.CO;2.

——, and ——, 1993: Kinematics and microphysics of the transition zone of the 10–11 June 1985 squall line. *J. Atmos. Sci.*, **50**, 3091–3110, doi:10.1175/1520-0469(1993)050<3091:KAMOTT>2.0.CO;2.

Bryan, G. H., and H. Morrison, 2012: Sensitivity of a simulated squall line to horizontal resolution and parameterization of microphysics. *Mon. Wea. Rev.*, **140**, 202–225, doi:10.1175/MWR-D-11-00046.1.

Chin, H.-N. S., 1994: The impact of the ice phase and radiation on a midlatitue squall line system. *J. Atmos. Sci.*, **51**, 3320–3343, doi:10.1175/1520-0469(1994)051<3320:TIOTIP>2.0.CO;2.

Dawson, D. T., II, M. Xue, J. A. Milbrandt, and M. K. Yau, 2010: Comparison of evaporation and cold pool development between single-moment and multimoment bulk microphysics schemes in idealized simulations of tornadic thunderstorms. *Mon. Wea. Rev.*, **138**, 1152–1171, doi:10.1175/2009MWR2956.1.

Evensen, G., 1994: Sequential data assimilation with a nonlinear quasi-geostrophic model using Monte Carlo methods to forecast error statistics. *J. Geophys. Res.*, **99**, 10 143–10 162, doi:10.1029/94JC00572.

Ferrier, B. S., 1994: A double-moment multiple-phase four-class bulk ice scheme. Part I: Description. *J. Atmos. Sci.*, **51**, 249–280, doi:10.1175/1520-0469(1994)051<0249:ADMMPF>2.0.CO;2.

——, W.-K. Tao, and J. Simpson, 1995: A double-moment multiple-phase four-class bulk ice scheme. Part II: Simulations of convective storms in different large-scale environments and comparisons with other bulk parameterizations. *J. Atmos. Sci.*, **52**, 1001–1033, doi:10.1175/1520-0469(1995)052<1001:ADMMPF>2.0.CO;2.

Fovell, R. G., and Y. Ogura, 1988: Numerical simulation of a midlatitude squall line in two dimensions. *J. Atmos. Sci.*, **45**, 3846–3879, doi:10.1175/1520-0469(1988)045<3846:NSOAMS>2.0.CO;2.

Gallus, W. A., Jr., and R. H. Johnson, 1995: The dynamics of circulations within the trailing stratiform region of squall lines. Part I: The 10–11 June PRE-STORM system. *J. Atmos. Sci.*, **52**, 2161–2187, doi:10.1175/1520-0469(1995)052<2161:TDOCWT>2.0.CO;2.

Gamache, J. F., and R. A. Houze Jr., 1982: Mesoscale air motions associated with a tropical squall line. *Mon. Wea. Rev.*, **110**, 118–135, doi:10.1175/1520-0493(1982)110<0118:MAMAWA>2.0.CO;2.

Gao, J.-D., and D. J. Stensrud, 2012: Assimilation of reflectivity data in a convective-scale, cycled 3DVAR framework with hydrometeor classification. *J. Atmos. Sci.*, **69**, 1054–1065, doi:10.1175/JAS-D-11-0162.1.

——, M. Xue, K. Brewster, and K. K. Droegemeier, 2004: A three-dimensional variational data analysis method with recursive filter for Doppler radars. *J. Atmos. Oceanic Technol.*, **21**, 457–469, doi:10.1175/1520-0426(2004)021<0457:ATVDAM>2.0.CO;2.

Grim, J. A., G. M. McFarquhar, R. M. Rauber, A. M. Smith, and B. F. Jewett, 2009: Microphysical and thermodynamic structure and evolution of the trailing stratiform regions of mesoscale convective systems during BAMEX. Part II: Column model simulations. *Mon. Wea. Rev.*, **137**, 1186–1205, doi:10.1175/2008MWR2505.1.

Houze, R. A., Jr., and D. D. Churchill, 1987: Mesoscale organization and cloud microphysics in a Bay of Bengal depression. *J. Atmos. Sci.*, **44**, 1845–1867, doi:10.1175/1520-0469(1987)044<1845:MOACMI>2.0.CO;2.

——, M. I. Biggerstaff, S. A. Rutledge, and B. F. Smull, 1989: Interpretation of Doppler weather radar displays of midlatitude mesoscale convective systems. *Bull. Amer. Meteor. Soc.*, **70**, 608–619, doi:10.1175/1520-0477(1989)070<0608:IODWRD>2.0.CO;2.

Hu, M., M. Xue, and K. Brewster, 2006a: 3DVAR and cloud analysis with WSR-88D level-II data for the prediction of Fort Worth tornadic thunderstorms. Part I: Cloud analysis and its impact. *Mon. Wea. Rev.*, **134**, 675–698, doi:10.1175/MWR3092.1.

——, ——, J. Gao, and K. Brewster, 2006b: 3DVAR and cloud analysis with WSR-88D level-II data for the prediction of Fort Worth tornadic thunderstorms. Part II: Impact of radial velocity analysis via 3DVAR. *Mon. Wea. Rev.*, **134**, 699–721, doi:10.1175/MWR3093.1.

Jung, Y., M. Xue, and G. Zhang, 2010: Simultaneous estimation of microphysical parameters and the atmospheric state using simulated polarimetric radar data and an ensemble Kalman filter in the presence of an observation operator error. *Mon. Wea. Rev.*, **138**, 539–562, doi:10.1175/2009MWR2748.1.

——, ——, and M. Tong, 2012: Ensemble Kalman filter analyses of the 29–30 May 2004 Oklahoma tornadic thunderstorm using one- and two-moment bulk microphysics schemes, with verification against polarimetric data. *Mon. Wea. Rev.*, **140**, 1457–1475, doi:10.1175/MWR-D-11-00032.1.

Kessler, E. I., 1969: *On the Distribution and Continuity of Water Substance in Atmospheric Circulations. Meteor. Monogr.*, No. 32, Amer. Meteor. Soc., 84 pp.

Lerach, D. G., S. A. Rutledge, C. R. Williams, and R. Cifelli, 2010: Vertical structure of convective systems during NAME 2004. *Mon. Wea. Rev.*, **138**, 1695–1714, doi:10.1175/2009MWR3053.1.

Lin, Y.-L., R. D. Farley, and H. D. Orville, 1983: Bulk parameterization of the snow field in a cloud model. *J. Climate Appl. Meteor.*, **22**, 1065–1092, doi:10.1175/1520-0450(1983)022<1065:BPOTSF>2.0.CO;2.

Marshall, J. S., and W. M. Palmer, 1948: The distribution of raindrops with size. *J. Meteor.*, **5**, 165–166, doi:10.1175/1520-0469(1948)005<0165:TDORWS>2.0.CO;2.

Meng, Z., F. Zhang, P. Markowski, D. Wu, and K. Zhao, 2012: A modeling study on the development of a bowing structure and associated rear inflow within a squall line over south China. *J. Atmos. Sci.*, **69**, 1182–1207, doi:10.1175/JAS-D-11-0121.1.

Milbrandt, J. A., and M. K. Yau, 2005a: A multimoment bulk microphysics parameterization. Part I: Analysis of the role of the spectral shape parameter. *J. Atmos. Sci.*, **62**, 3051–3064, doi:10.1175/JAS3534.1.

——, and ——, 2005b: A multimoment bulk microphysics parameterization. Part II: A proposed three-moment closure and scheme description. *J. Atmos. Sci.*, **62**, 3065–3081, doi:10.1175/JAS3535.1.

Moncrieff, M. W., 1978: The dynamical structure of two-dimensional steady convection in constant vertical shear. *Quart. J. Roy. Meteor. Soc.*, **104**, 543–567, doi:10.1002/qj.49710444102.

Morrison, H., G. Thompson, and V. Tatarskii, 2009: Impact of cloud microphysics on the development of trailing stratiform precipitation in a simulated squall line: Comparison of one- and two-moment schemes. *Mon. Wea. Rev.*, **137**, 991–1007, doi:10.1175/2008MWR2556.1.

Pan, Y., K. Zhao, Y. Pan, and Y. Wang, 2012: Dual-Doppler analysis of a squall line in southern China (in Chinese). *Acta Meteor. Sin.*, **70**, 736–735.

Parker, M. D., and R. H. Johnson, 2000: Organizational modes of midlatitude mesoscale convective systems. *Mon. Wea. Rev.*, **128**, 3413–3436, doi:10.1175/1520-0493(2001)129<3413:OMOMMC>2.0.CO;2.

Rogers, R. R., and M. K. Yau, 1989: *A Short Course in Cloud Physics.* 3rd ed. Pergamon Press, 293 pp.

Rotunno, R., W. C. Skamarock, and C. Snyder, 1998: Effects of surface drag on fronts within numerically simulated baroclinic waves. *J. Atmos. Sci.*, **55**, 2119–2129, doi:10.1175/1520-0469(1998)055<2119:EOSDOF>2.0.CO;2.

Rowe, A. K., S. A. Rutledge, and T. J. Lang, 2012: Investigation of microphysical processes occurring in organized convection during NAME. *Mon. Wea. Rev.*, **140**, 2168–2187, doi:10.1175/MWR-D-11-00124.1.

Rutledge, S. A., and R. A. Houze Jr., 1987: A diagnostic modeling study of the trailing stratiform region of a midlatitude squall line. *J. Atmos. Sci.*, **44**, 2640–2656, doi:10.1175/1520-0469(1987)044<2640:ADMSOT>2.0.CO;2.

Schenkman, A., M. Xue, A. Shapiro, K. Brewster, and J. Gao, 2011: The analysis and prediction of the 8–9 May 2007 Oklahoma tornadic mesoscale convective system by assimilating WSR-88D and CASA radar data using 3DVAR. *Mon. Wea. Rev.*, **139**, 224–246, doi:10.1175/2010MWR3336.1.

Smith, A. M., G. M. McFarquhar, R. M. Rauber, J. A. Grim, M. S. Timlin, B. F. Jewett, and D. P. Jorgensen, 2009: Microphysical and thermodynamic structure and evolution of the trailing stratiform regions of mesoscale convective systems during BAMEX. Part I: Observations. *Mon. Wea. Rev.*, **137**, 1165–1185, doi:10.1175/2008MWR2504.1.

Smith, P. L., Jr., C. G. Myers, and H. D. Orville, 1975: Radar re-flectivity factor calculations in numerical cloud models using bulk parameterization of precipitation processes. *J. Appl. Meteor.*, **14**, 1156–1165, doi:10.1175/1520-0450(1975)014<1156:RRFCIN>2.0.CO;2.

Smull, B. F., and R. A. Houze Jr., 1985: A midlatitude squall line with a trailing region of stratiform rain: Radar and satellite observations. *Mon. Wea. Rev.*, **113**, 117–133, doi:10.1175/1520-0493(1985)113<0117:AMSLWA>2.0.CO;2.

Straka, J. M., M. S. Gilmore, K. M. Kanak, and E. N. Rasmussen, 2005: A comparison of the conservation of number concen-tration for the continuous collection and vapor diffusion growth equations using one- and two-moment schemes. *J. Appl. Me-teor.*, **44**, 1844–1849, doi:10.1175/JAM2314.1.

Sun, J., and N. A. Crook, 1997: Dynamical and microphysical re-trieval from Doppler radar observations using a cloud model and its adjoint. Part I: Model development and simulated data experiments. *J. Atmos. Sci.*, **54**, 1642–1661, doi:10.1175/1520-0469(1997)054<1642:DAMRFD>2.0.CO;2.

——, and ——, 1998: Dynamical and microphysical retrieval from Doppler radar observations using a cloud model and its ad-joint. Part II: Retrieval experiments of an observed Florida convective storm. *J. Atmos. Sci.*, **55**, 835–852, doi:10.1175/1520-0469(1998)055<0835:DAMRFD>2.0.CO;2.

Szeto, K. K., and H.-R. Cho, 1994a: A numerical investigation of squall lines. Part II: The mechanics of evolution. *J. Atmos. Sci.*, **51**, 425–433, doi:10.1175/1520-0469(1994)051<0425:ANIOSL>2.0.CO;2.

——, and ——, 1994b: A numerical investigation of squall lines. Part III: Sensitivity to precipitation processes and the Coriolis force. *J. Atmos. Sci.*, **51**, 1341–1351, doi:10.1175/1520-0469(1994)051<1341:ANIOSL>2.0.CO;2.

Tong, M., and M. Xue, 2005: Ensemble Kalman filter assimilation of Doppler radar data with a compressible nonhydrostatic model: OSS experiments. *Mon. Wea. Rev.*, **133**, 1789–1807, doi:10.1175/MWR2898.1.

——, and ——, 2008a: Simultaneous estimation of microphysical parameters and atmospheric state with radar data and en-semble square-root Kalman filter. Part I: Sensitivity analysis and parameter identifiability. *Mon. Wea. Rev.*, **136**, 1630–1648, doi:10.1175/2007MWR2070.1.

——, and ——, 2008b: Simultaneous estimation of microphysical parameters and atmospheric state with radar data and ensem-ble square-root Kalman filter. Part II: Parameter estimation experiments. *Mon. Wea. Rev.*, **136**, 1649–1668, doi:10.1175/2007MWR2071.1.

Ulbrich, C. W., 1983: Natural variations in the analytical form of the raindrop size distribution. *J. Climate Appl. Meteor.*, **22**, 1764–1775, doi:10.1175/1520-0450(1983)022<1764:NVITAF>2.0.CO;2.

van den Heever, S. C., and W. R. Cotton, 2004: The impact of hail size on simulated supercell storms. *J. Atmos. Sci.*, **61**, 1596–1609, doi:10.1175/1520-0469(2004)061<1596:TIOHSO>2.0.CO;2.

Van Weverberg, K., and Coauthors, 2013: The role of cloud mi-crophysics parameterization in the simulation of mesoscale convective system clouds and precipitation in the tropical western Pacific. *J. Atmos. Sci.*, **70**, 1104–1128, doi:10.1175/JAS-D-12-0104.1.

Wainwright, C. E., D. T. Dawson II, M. Xue, and G. Zhang, 2014: Diagnosing the intercept parameters of the expo-nential drop size distributions in a single-moment micro-physics scheme and impact on supercell storm simulations. *J. Appl. Meteor. Climatol.*, **53**, 2072–2090, doi:10.1175/JAMC-D-13-0251.1.

Weisman, M. L., and R. Rotunno, 2004: ''A theory for strong long-lived squall lines'' revisited. *J. Atmos. Sci.*, **61**, 361–382, doi:10.1175/1520-0469(2004)061<0361:ATFSLS>2.0.CO;2.

Xu, J.-L., 1983: Some hail research in China. *Bull. Amer. Meteor. Soc.*, **64**, 124–132, doi:10.1175/1520-0477(1983)064<0124:SHRIC>2.0.CO;2.

Xue, M., K. K. Droegemeier, and V. Wong, 2000: The Advanced Regional Prediction System (ARPS)—A multiscale non-hydrostatic atmospheric simulation and prediction tool. Part I: Model dynamics and verification. *Meteor. Atmos. Phys.*, **75**, 161–193, doi:10.1007/s007030070003.

——, and Coauthors, 2001: The Advanced Regional Prediction System (ARPS)—A multiscale nonhydrostatic atmospheric simulation and prediction tool. Part II: Model physics and ap-plications. *Meteor. Atmos. Phys.*, **76**, 143–165, doi:10.1007/s007030170027.

——, D.-H. Wang, J.-D. Gao, K. Brewster, and K. K. Droegemeier, 2003: The Advanced Regional Prediction System (ARPS), storm-scale numerical weather prediction and data assim-ilation. *Meteor. Atmos. Phys.*, **82**, 139–170, doi:10.1007/s00703-001-0595-6.

——, Y. Jung, and G. Zhang, 2010: State estimation of convec-tive storms with a two-moment microphysics scheme and an ensemble Kalman filter: Experiments with simulated radar data. *Quart. J. Roy. Meteor. Soc.*, **136**, 685–700, doi: 10.1002/qj.593.

——, F. Kong, K. W. Thomas, J. Gao, Y. Wang, K. Brewster, and K. K. Droegemeier, 2013: Prediction of convective storms at convection-resolving 1 km resolution over continental United States with radar data assimilation: An example case of 26 May 2008 and precipitation forecasts from spring 2009. *Adv. Meteor.*, **2013**, 259052, doi:10.1155/2013/259052.

Zhang, G., M. Xue, Q. Cao, and D. Dawson, 2008: Diagnosing the intercept parameter for exponential raindrop size distribution based on video disdrometer observations: Model develop-ment. *J. Appl. Meteor. Climatol.*, **47**, 2983–2992, doi:10.1175/2008JAMC1876.1.

Zipser, E. J., 1977: Mesoscale and convective-scale downdrafts as distinct components of squall-line circulation. *Mon. Wea. Rev.*, **105**, 1568–1589, doi:10.1175/1520-0493(1977)105<1568:MACDAD>2.0.CO;2.